BAMS Article

Chasing Snowstorms

The Investigation of Microphysics and Precipitation for Atlantic Coast-Threatening Snowstorms (IMPACTS) Campaign

Lynn A. McMurdie, Gerald M. Heymsfield, John E. Yorks, Scott A. Braun, Gail Skofronick-Jackson, Robert M. Rauber, Sandra Yuter, Brian Colle, Greg M. McFarquhar, Michael Poellot, David R. Novak, Timothy J. Lang, Rachael Kroodsma, Matthew McLinden, Mariko Oue, Pavlos Kollias, Matthew R. Kumjian, Steven J. Greybush, Andrew J. Heymsfield, Joseph A. Finlon, Victoria L. McDonald, and Stephen Nicholls

ABSTRACT: The Investigation of Microphysics and Precipitation for Atlantic Coast-Threatening Snowstorms (IMPACTS) is a NASA-sponsored field campaign to study wintertime snowstorms focusing on East Coast cyclones. This large cooperative effort takes place during the winters of 2020–23 to study precipitation variability in winter cyclones to improve remote sensing and numerical forecasts of snowfall. Snowfall within these storms is frequently organized in banded structures on multiple scales. The causes for the occurrence and evolution of a wide spectrum of snowbands remain poorly understood. The goals of IMPACTS are to characterize the spatial and temporal scales and structures of snowbands, understand their dynamical, thermodynamical, and microphysical processes, and apply this understanding to improve remote sensing and modeling of snowfall. The first deployment took place in January–February 2020 with two aircraft that flew coordinated flight patterns and sampled a range of storms from the Midwest to the East Coast. The satellite-simulating ER-2 aircraft flew above the clouds and carried a suite of remote sensing instruments including cloud and precipitation radars, lidar, and passive microwave radiometers. The in situ P-3 aircraft flew within the clouds and sampled environmental and microphysical quantities. Ground-based radar measurements from the National Weather Service network and a suite of radars located on Long Island, New York, along with supplemental soundings and the New York State Mesonet ground network provided environmental context for the airborne observations. Future deployments will occur during the 2022 and 2023 winters. The coordination between remote sensing and in situ platforms makes this a unique publicly available dataset applicable to a wide variety of interests.

KEYWORDS: Cloud microphysics; Freezing precipitation; Mesoscale processes; Aircraft observations; In situ atmospheric observations; Remote sensing

https://doi.org/10.1175/BAMS-D-20-0246.1
Corresponding author: Lynn A. McMurdie, lynnm@uw.edu
Supplemental material: https://doi.org/10.1175/BAMS-D-20-0246.2

In final form 11 February 2022

AFFILIATIONS: McMurdie, Finlon, and McDonald—Department of Atmospheric Sciences, University of Washington, Seattle, Washington; **G. M. Heymsfield, Yorks, Braun, and McLinden**—NASA Goddard Space Flight Center, Greenbelt, Maryland; **Skofronick-Jackson***—NASA Earth Sciences Division, Washington, D.C.; **Rauber**—Department of Atmospheric Sciences, University of Illinois at Urbana–Champaign, Urbana, Illinois; **Yuter**—Department of Marine, Earth and Atmospheric Sciences, North Carolina State University, Raleigh, North Carolina; **Colle, Oue, and Kollias**—Division of Atmospheric Sciences, Stony Brook University, State University of New York, Stony Brook, New York; **McFarquhar**—Cooperative Institute for Severe and High Impact Weather Research and Operations, and School of Meteorology, University of Oklahoma, Norman, Oklahoma; **Poellot**—Department of Atmospheric Sciences, University of North Dakota, Grand Forks, North Dakota; **Novak**—Weather Prediction Center, NOAA/NWS/NCEP, College Park, Maryland; **Lang**—NASA Marshall Space Flight Center, Huntsville, Alabama; **Kroodsma**—NASA Goddard Space Flight Center, Greenbelt, and Earth System Science Interdisciplinary Center, University of Maryland, College Park, College Park, Maryland; **Kumjian and Greybush**—Department of Meteorology and Atmospheric Science, The Pennsylvania State University, University Park, Pennsylvania; **A. J. Heymsfield**—National Center for Atmospheric Research, Boulder, Colorado; **Nicholls**—Science Systems and Applications, Inc., Lanham, Maryland
***Deceased.**

Winter snowstorms impact large populations, affecting as many as 100 million people in major urban corridors along the eastern seaboard of the United States, and covering over one million square kilometers (or 400,000 square miles; Kocin and Uccellini 2004). Snowy conditions contribute to flight cancellations, power grid outages, school and business closings, and a multitude of vehicle crashes, injuries, and fatalities annually in the United States, primarily in the Northeast and Midwest (Black and Mote 2015; Guarino and Firestine 2010; Hines et al. 2009; Pisano et al. 2008). Economic impacts on individual states can be as much as \$300–\$700 million per snow-shutdown day (IHS Global Insight 2014). The mesoscale variability in precipitation type, snowfall rates, and amounts presents a major challenge to operational forecasters (Nicosia and Grumm 1999; Kocin and Uccellini 2004). Substantial errors in forecasts of precipitation type and quantity can result from relatively small errors (~100–200 km) of the forecast rain–snow line, small forecast errors of the location of bands of higher intensity snowfall, or inadequate characterization of the microphysical growth regimes within numerical models (Zhang et al. 2002; Ganetis and Colle 2015; Greybush et al. 2017; Connelly and Colle 2019; Radford et al. 2019). Improving the understanding of snowfall processes and prediction of snowfall amounts, intensity, timing, and distribution will have broad societal and economic benefits.

Snowfall accumulations can range from a few millimeters to up to a meter over a relatively short distance during a single storm event, even in the absence of strong terrain influences (e.g., Picca et al. 2014). Figure 1 demonstrates this strong mesoscale variability of snowfall for a storm that occurred 1–2 February 2021. The 24-h snowfall totals ranged from less than 0.25 cm (<0.1 in.) over portions of Ohio, western New York, and Pennsylvania to 45–60 cm (1.5–2 ft) over portions of New York, Connecticut, and Massachusetts. This mesoscale variability in location, type, and intensity of precipitation often results from precipitation banding (e.g., Houze et al. 1976; Matejka et al. 1980; Sanders and Bosart 1985; Wolfsberg et al. 1986; Geerts and Hobbs 1991; Jurewicz and Evans 2004; Novak et al. 2004, 2008, 2010; Griffin et al. 2014; Picca et al. 2014; Ganetis et al. 2018). The processes contributing to the observed precipitation banding in winter cyclones vary widely on temporal and spatial scales.

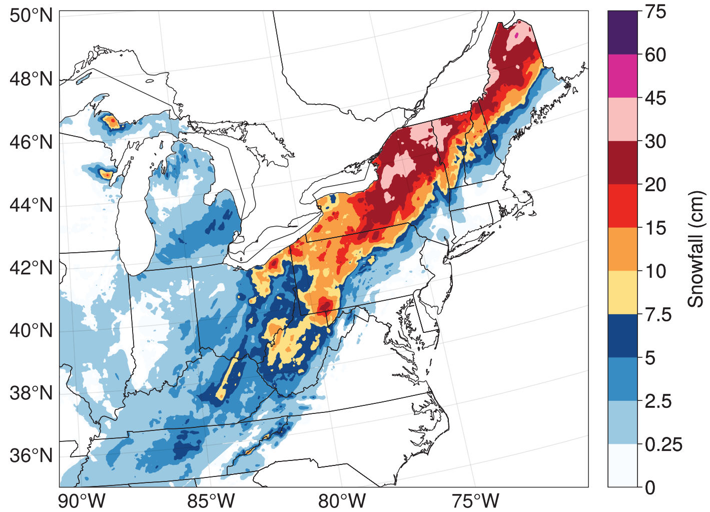

Fig. 1. Snowfall totals in centimeters for the period 1200 UTC 1–1200 UTC 2 Feb 2021. Data source: National Operational Hydrologic Remote Sensing Center snowfall analysis version 2 obtained from www.nohrsc.noaa.gov/snowfall_v2/**.**

The larger-scale, or primary, bands are most likely associated with midlevel frontogenesis processes (e.g., Novak et al. 2004, 2008), and have been associated with a spectrum of instabilities, such as conditional symmetric instability (e.g., Schultz and Schumacher 1999), conditional instability (e.g., Trapp et al. 2001; Morales 2008), and inertial instability (e.g., Jurewicz and Evans 2004; Schultz and Knox 2007). Ganetis et al. (2018) showed that sets of roughly parallel mesoscale bands occurred in a wide range of frontogenesis and moist potential vorticity environments. Possible mechanisms associated with mesoscale multibanded structures include elevated convection, generating cells, shear instabilities, and gravity wave activity (Bosart and Sanders 1986; Zhang et al. 2001, 2003; Kumjian et al. 2014; Plummer et al. 2014, 2015; Rauber et al. 2014, 2017; Rosenow et al. 2014, 2018; Keeler et al. 2016a,b, 2017; Lackmann and Thompson 2019), as illustrated in Fig. 2. Numerical models often fail to realistically predict the spectrum of snowbands in winter storms, possibly because of incomplete representations of snow growth processes and flow deformation fields (Connelly and Colle 2019; Harrington et al. 2013a,b; Jensen et al. 2017). Major aspects of snowbands at all scales remain poorly understood, such as how bands are initiated and organized, how the vertical variability of horizontal and vertical motions and thermodynamic instabilities translate to increased snowfall rates at the surface, and how the environmental and microphysical properties vary within and outside of snowbands.

Many regions across the globe lack direct measurements of precipitation or adequate radar coverage. Their remote locations (e.g., mountainous, oceanic, or polar regions) make surface measurements of precipitation difficult or impossible. These limitations highlight the importance of satellite-based global precipitation data especially for monitoring and predicting precipitation distribution in winter cyclones. The current NASA Global Precipitation Measurement (GPM) mission (Hou et al. 2014; Skofronick-Jackson et al. 2017) includes a state-of-the-art *Core Observatory* flying at an inclined non–sun synchronous orbit equipped with the first spaceborne multiple-frequency radar, the Dual-Frequency Precipitation Radar (DPR), and a multifrequency passive microwave radiometer, the GPM Microwave Imager (GMI). The 2017–27 Decadal Survey for Earth Science and Applications from Space (NASEM 2018) calls for a future mission with radars and multifrequency passive microwave and submillimeter radiometers, which led to the recent development of the NASA Earth System Observatory (ESO) Atmosphere Observing System (AOS) mission to address science goals related to clouds, convection, and precipitation. Although a key GPM objective is to detect and measure falling snow at the surface over a wide range of snowfall intensities, the current GPM algorithms are limited by

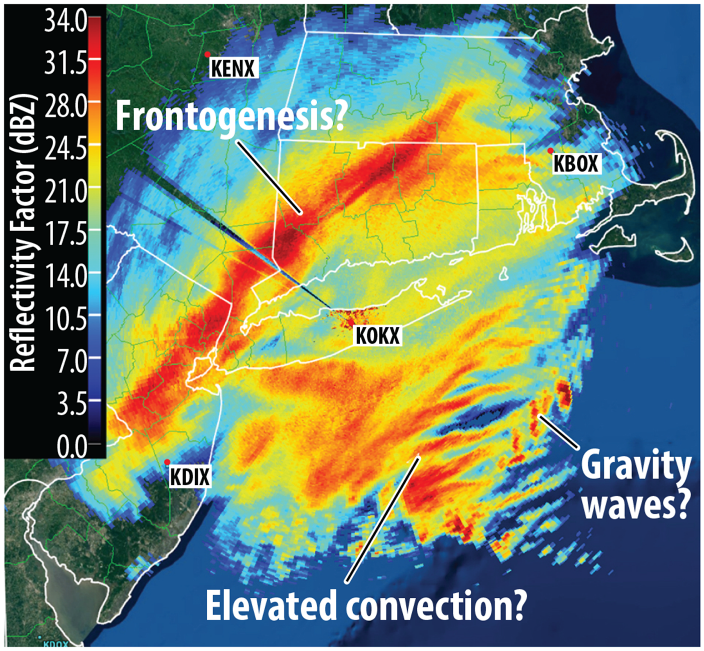

Fig. 2. An example plot of radar reflectivity factor (dB*Z*) illustrating narrow regions of high reflectivity associated with the primary snowband and multibands. Potential mechanisms contributing to snowband formation and maintenance are indicated on the figure.

rather large uncertainties in snow amounts (Skofronick-Jackson et al. 2017). Challenges facing remote sensing of snow include, among others, attenuation, scattering from complex particle geometries, variations in particle densities, partially melted and mixed-phase particles, and presence of supercooled liquid water. To address these challenges and improve retrievals for future missions such as ESO/AOS, concurrent measurements by remote sensing instruments at the same frequencies of spaceborne instruments, such as the DPR and GMI, together with in situ microphysical measurements of particle geometries and intrinsic properties (e.g., ice water content, cloud liquid water) and environmental variables are necessary.

The Investigation of Microphysics and Precipitation of Atlantic Coast-Threatening Snowstorms (IMPACTS) is a current NASA Earth Venture Suborbital-3 (EVS-3) field campaign to improve the understanding of snowfall processes, remote sensing of snow, and the prediction of banded structure and evolution. It is the first major field study to focus on precipitation processes in winter storms along the U.S. East Coast in over 30 years [e.g., see Dirks et al. (1988) and Hadlock and Kreitzberg (1988) for description of the earlier campaigns]. IMPACTS takes place over three winter seasons, with the first deployment completed during January–February 2020. Two additional deployments are planned for winters 2022 and 2023. IMPACTS science objectives as illustrated in Fig. 3 are to 1) characterize the spatial and temporal scales of snowband structures in winter storms; 2) understand the dynamical, thermodynamical, and microphysical process that produce snowband structures; and 3) apply this understanding of the structures and underlying processes to improve remote sensing and modeling of snowfall. IMPACTS is designed to achieve these goals through coordinated flights using aircraft equipped with instruments ideally suited to study mixed-phase clouds, augmented with ground-based radar, rawinsonde and surface observations, data from multiple NASA and NOAA satellites, and regional analyses and convection-permitting short-term forecasts.

IMPACTS observational strategy

The primary observing platforms for IMPACTS are two instrumented aircraft that observe storms of interest: the "satellite-simulating" ER-2, which flies high above the storms equipped with passive and active remote sensing instruments at the same or similar frequencies as

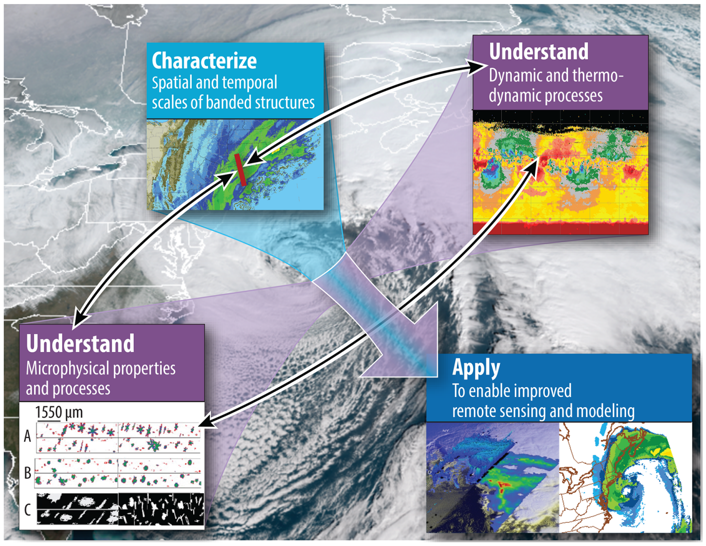

Fig. 3. IMPACTS goals illustrated through graphics overlaying an intense winter cyclone over the North Atlantic.

instruments flown on precipitation measuring satellites; and the “cloud-penetrating” P-3, which flies within clouds equipped with microphysical probes and environmental measuring instrumentation. The combination of remote sensing observations that provide detailed horizontal and vertical measurements of precipitation structures and collocated microphysical measurements addresses IMPACTS goals to characterize and understand snowband structure and apply this understanding to improving remote sensing and modeling. Due to the long flight duration capabilities of each aircraft, IMPACTS is able to sample snowstorms over a large geographical region, spanning from the Midwest to the East Coast, as illustrated in Fig. 4 for the winter 2020 deployment season. This allows a variety of storms to be sampled, does not limit operations to a small area due to dependence on ground instruments deployed in one location, and allows for observations of snow outside the East Coast if snow conditions are infrequent along the coastal region in a season, as was sometimes the case in 2020.

The ER-2 serves as an advanced cloud and precipitation remote sensing platform capable of simulating satellite sensors, but with a much higher spatial and temporal resolution. By using an aircraft platform, sampling across snowband structures multiple times in the same storm is possible and is not limited to when a satellite passes over a storm. The instrumentation includes multiple-frequency Doppler radars (W, Ka, Ku, and X band) and passive microwave radiometers at a range of frequencies, a cloud lidar and a lightning sensor array (see Table 1 for the list of instruments deployed during the 2020 winter season). The range of radar frequencies provides high sensitivity to cloud tops and light snowfall (W and Ka bands) and relative insensitivity to attenuation in heavy snowfall (Ku and X bands). The nadir sampling by the radars provides high vertical resolution of the cloud systems, and the Doppler capabilities of all the radars allow the ability to detect vertical motions across the storms both within and outside of snowbands. The microwave radiometers provide horizontal sampling and span a range of frequencies for measuring rain and snowfall over land and water. Horizontal winds can be retrieved utilizing the conically scanning ability of the X-band radar for 2D winds (e.g., Helms et al. 2020) and 3D winds (Guimond et al. 2014). The lidar provides the highest possible sensitivity to thin clouds and enables detection of supercooled liquid water in generating cells near cloud tops (McGill et al. 2004). Airborne radar, radiometer, and lidar observations can be used in various retrievals to provide particle size and other microphysical information (e.g., Grecu et al. 2018; Chase et al. 2018; Mitrescu et al. 2005). The Lightning Instrument Package (LIP) measures the electric field and changes due to lightning occurrence (Schultz et al. 2021).

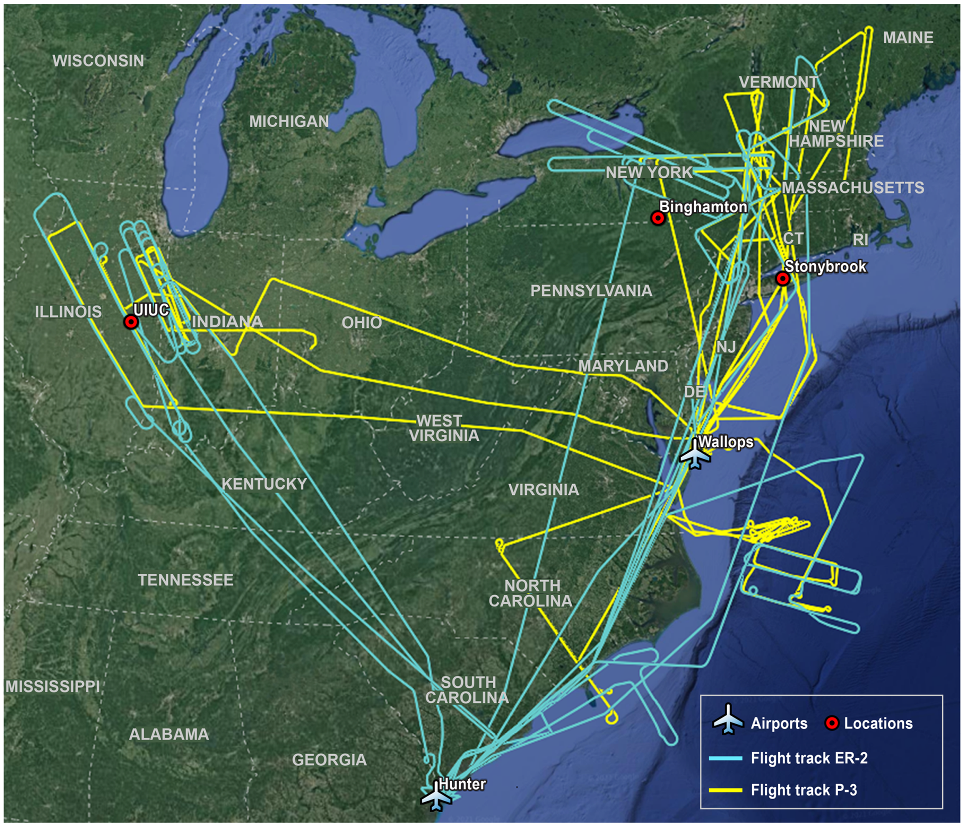

Maps data: Google Landsat / Copernicus Data SIO, NOAA, U.S. Navy, NGA, GEBCO INEGI Data LDEO-Columbia, NSF, NOAA

Fig. 4. Flight tracks of the ER-2 (blue) and P-3 (yellow) during the 2020 IMPACTS deployment. Airplane symbols indicate airfields used in 2020, Wallops (P-3) and Hunter (ER-2). Red dots indicate home-base locations used for mobile sounding launches.

The P-3 serves as an in situ platform for sampling microphysical particle characteristics, the local environment of the particles, and the vertical thermodynamic and kinematic profiles from dropsondes (see Table 2 for the list of instruments and their characteristics for the 2020 deployment). Multiple probes measure microphysical properties such as liquid water content, total water content, particle size and shape, and the presence of supercooled liquid water across a wide range of particle sizes, from small cloud particles (2 μm) to large crystal aggregates (10 cm). The Turbulent Air Motion Measurement System (TAMMS) gives the high-resolution flight-level 3D-wind field, temperature, and humidity, and when flights are over open ocean, dropsondes are launched to obtain vertical profiles of pressure, temperature, relative humidity, and winds. These in situ measurements provide critical cloud and snowband structure information, and, when combined with the remote sensing information from the ER-2 instrument suite, data from the operational National Weather Service (NWS) Weather Surveillance Radar 1988-Doppler (WSR-88D) radar network, ground-based remote and meteorological sensors, and special rawinsondes, provide measurements critical for improving satellite snowfall retrieval algorithms.

The two aircraft fly in approximately vertically stacked, coordinated patterns (Fig. 5) with flight legs generally orthogonal to the snowband orientation. The P-3 samples at different altitudes to capture the vertical structure and temperature dependence of microphysical properties, from which information about microphysical processes, such as rapid crystal growth by vapor deposition (from −10° to −20°C; Rogers and Yau 1989), peaks in aggregation efficiency (from −12.5° to −17°C and from −4° to −6°C; Mitchell 1988; McFarquhar et al. 2007), and secondary ice production processes (<−10°C; Field et al. 2017) can be inferred. The warmer temperature ranges (~−5°C) may at times be below the minimum flight altitude for the P-3 (roughly 1.5 km, varying regionally over land), so may not always be sampled. Ice nucleation

Table 1. Instruments flown on the ER-2 during the 2020 IMPACTS deployment.

Instrument—PI/organization	Instrument characteristics	Derived data products	Reference
Advanced Microwave Precipitation Radiometer (AMPR)—T. Lang/MSFC	Cross-track scanning microwave radiometer at 10, 19, 37, and 85 GHz	Precipitation characteristics, path integrated LWC and IWC	Spencer et al. (1994), Amiot et al. (2021)
Cloud Physics Lidar (CPL)—M. McGill/GSFC	Attenuated backscatter at 355, 532, and 1,064 nm; volume depolarization ratio at 1,064 nm	Cloud/aerosol layer boundaries, cloud/aerosol optical depth, extinction, and depolarization; detection of cloud phase at cloud top	McGill et al. (2002)
Cloud Radar System (CRS)—M. McLinden/GSFC	W-band nadir-pointing Doppler radar with minimum detectable threshold of −30 dB*Z* at 10-km altitude; linear depolarization	Vertical velocity, precipitation rates, phase, hydrometeor size, various vertical profile characteristics	Walker McLinden et al. (2021)
Conical Scanning Millimeter-wave Imaging Radiometer (CoSMIR)—R. Kroodsma/GSFC	Conical and/or cross-track scanning passive microwave radiometer at ~50, 89, 165.5, and 183 GHz	Precipitation characteristics, path integrated LWC and IWC	Kroodsma et al. (2019)
ER-2 X-Band Doppler Radar (EXRAD)—G. Heymsfield/GSFC	X-band nadir and conical scanning Doppler radar with minimum detectable threshold of −12 dB*Z*/−3 dB*Z* (nadir/scanning) at 10-km range	Vertical velocity, precipitation rates, phase, hydrometeor size, various vertical profile characteristics, horizontal winds	See McMurdie et al. (2019) for instrument dataset
High-altitude Imaging Wind and Rain Airborne Profiler (HIWRAP)—L. Li/GSFC	Ku- and Ka-band nadir-pointing Doppler radars with minimum detectable threshold of −10 dB*Z* (Ku) and −12 dB*Z* (Ka) at 10-km altitude; linear depolarization	Vertical velocity, precipitation rates, phase, hydrometeor size, various vertical profile characteristics	Li et al. (2015)
Lightning Instrument Package (LIP)—C. Schultz/MSFC	Electric field	Vector electric field and changes due to lightning occurrence	Mach et al. (2009)

often occurs at much colder temperatures that are typically above the maximum flight altitude of the P-3 (7–8.5 km depending on fuel load), so is not a focus for IMPACTS. The ER-2 cruise speed is approximately 205 m s^{-1} and the P-3 speed ranges between 140 and 160 m s^{-1} depending on altitude. Because the aircraft cruise speed differs, the ER-2 flight legs are longer than the P-3's to compensate. The legs are timed so that the aircraft are vertically aligned at the center of each flight track and the time difference between the two aircraft at the end of the legs is no more than 5 min. This space/time differential at the end of the flight legs can introduce some uncertainty relating the microphysical properties to radar measurements especially for the small-scale features, but is within minimum distance and time criteria used in previous studies (Heymsfield et al. 2016; Chase et al. 2018; Finlon et al. 2019; Ding et al. 2020; Duffy et al. 2021). The typical flight patterns during IMPACTS primarily consist of a single repeated track, a racetrack, or lawn-mower type patterns depending on storm movement and available flight corridors (Fig. 4).

Although IMPACTS is primarily an aircraft-based field campaign, ground-based observing networks augment the aircraft observations and are critical to achieve IMPACTS goals (Fig. 3). By focusing on the northeast and midwest United States, IMPACTS takes advantage of the NOAA observing infrastructure including the rawinsonde network, NWS Automated Surface Observing System (ASOS) surface meteorological stations, and the WSR-88D radar sites. These radars provide large-scale context on the horizontal structure and movement of snowbands, but lack the vertical resolution necessary to diagnose the range of processes that may be contributing to snowband formation, evolution, and structure; thus, the need

Table 2. Instruments flown on the P-3 during the 2020 IMPACTS deployment.

Instrument—PI/organization	Instrument characteristics	Derived data products	Reference
Turbulent Air Motion Measurement System (TAMMS)—K. Thornhill/LaRC	In situ measurement systems designed to acquire high-frequency state parameters	Flight level 3D-wind vector, temperature, humidity	Barrick et al. (1996)
Advanced Vertical Atmospheric Profiling System (AVAPS)—K. Thornhill/LaRC	Expendable GPS-tracked device dropped from aircraft to measure in situ profiles	Vertical profiles of pressure, temperature, relative humidity, and winds	Hock and Franklin (1999)
Cloud-Droplet Probe (CDP)—M. Poellot/UND	Particle samples in 2–50-μm size range	Concentration and size distribution of cloud droplets	Lance et al. (2010)
Particle Habit Imaging and Polar Scattering (PHIPS)—M. Schnaiter/KIT	High resolution particle information up to ~700-μm size range	2D particle images, single particle phase discrimination and particle size distribution up to ~700-μm size range	Abdelmonem et al. (2016), Waitz et al. (2020)
2D-Stereo Probe (2DS)—M. Poellot/UND	Particle samples in 10-μm–3-mm size range	Droplet, ice particle size distributions, 3D particle images	Lawson et al. (2006)
High-Volume Precipitation Spectrometer-3 (HVPS-3)—M. Poellot/UND	Particle samples in 150-μm–10-cm size range	Droplet, ice particle size distributions, 2D projections of 3D particle images	Lawson et al. (1998)
Nevzorov Probe—M. Poellot/UND	Cloud liquid and total condensate up to 2 g m^{-3}	Liquid and ice water content	Korolev et al. (1998)
King Probe—M. Poellot/UND	Liquid water probe, up to 2 g m^{-3}, for cloud droplet sizes of 2–30 μm	Liquid water content	King et al. (1978)
Hawkeye Probe—M. Poellot/UND	Multiprobe sensor (FastCDP, 2DS, CPI)	Droplet, ice particle size distributions, 3D particle images	See McMurdie et al. (2019) for instrument dataset
Rosemont Icing Detector (RICE)—M. Poellot/UND	Supercooled liquid water measurements in excess of 0.01 g m^{-3}	Presence and approximate amount of supercooled liquid water	Claffey et al. (1995)
Water Isotope System for Precipitation and Entrainment Research (WISPER)—D. Toohey/U. Colo	Total ice measurements up to 2 g m^{-3}	Cloud particle concentration, condensate mass, water vapor, ice water content	Herman et al. (2020)

for aircraft observations. Vertical profiles of temperature, humidity, and winds from rawinsonde launches provide the environmental context of snowband structure. During IMPACTS operations, additional rawinsonde launches up to 3-hourly frequency are launched at NWS rawinsonde operational sites near the planned aircraft flight tracks. In addition, 2–3 mobile sounding teams launch soundings at locations determined by the flight-planning mission scientists. Locations used during the 2020 deployment were at Stony Brook, Long Island, University of Illinois at Urbana–Champaign, and Binghamton, New York (Fig. 4). The Binghamton, New York, team traveled to multiple locations throughout the northeast United States during 2020, whereas the Stony Brook team remained on Long Island (see "Early career and student participation" sidebar). Both teams, and a team from Millersville University, will be fully mobile in 2022 and 2023.

When storms of interest occur near Long Island, New York, the well-instrumented ground site at Stony Brook University (SBU) contributes important observations of snowbands (https://you.stonybrook.edu/radar/). This facility includes multiple radars, profiling microwave radiometers, a scanning Doppler lidar, and Parsivel disdrometers (see Table 3). The X-band, phased-array radar (SKYLER) is mounted on a mobile truck and can be positioned strategically to sample storms of interest. During the 2020 deployment, SKYLER remained on Long

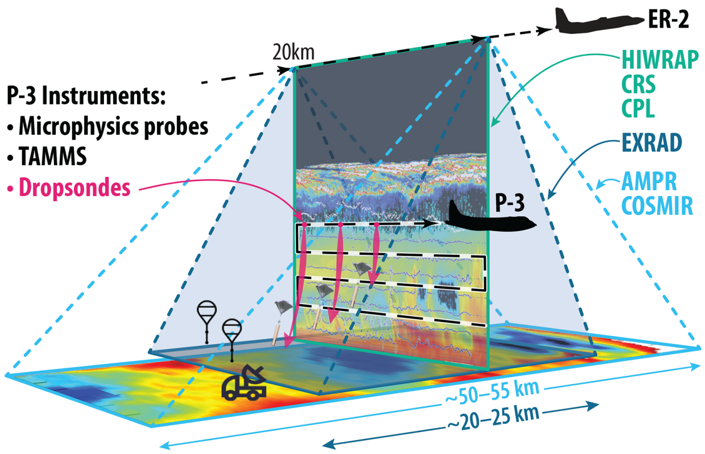

Fig. 5. Illustration of the observational strategy for IMPACTS. The satellite-simulating ER-2 flies above the storm and samples with passive and active remote sensing instruments (sampling width of the different instruments indicated with dashed colored lines; see Table 1 for list of instruments) while the P-3 flies within the storm at different altitudes, releasing dropsondes over water. Surface radars and mobile soundings are represented by the balloons and truck symbols.

Island, but in subsequent deployments, this facility will deploy to other locations within a 300-km radius of SBU to better sample storms where they occur.

In addition to the ASOS NWS surface observations of standard meteorological variables, data from the New York State Mesonet observing network are also part of the IMPACTS observing strategy (Brotzge et al. 2020). The New York Mesonet consists of 126 surface weather stations (standard meteorological variables, gauge measurements of the liquid equivalent of falling precipitation, and snow depth) and 17 sites with profiling lidars (up to 3 km) and microwave radiometers (temperature and humidity up to 10 km). In addition, 20 surface sites provide snow liquid equivalent measurements. More information about the New York Mesonet is given at www.nysmesonet.org and Brotzge et al. (2020).

High-resolution numerical modeling is integral to IMPACTS, both in terms of forecast support for operations and for addressing the science goals. During the 2020 deployment year, high-resolution regional model runs with varying initial conditions focused on the northeast United States were run by SBU and the NWS in real time to support operational decisions. During the data analysis phase, model runs will first be evaluated against the observed thermodynamic profiles and precipitation structures from radar, including dual-pol radar estimates of hydrometeor type, and inferred regions of aggregation and riming within the cloud. Then, model microphysics schemes will be evaluated and compared to measurements by the P-3 microphysical probes such as ice water content and derived quantities as well as compared to ground-based estimates of the fall speeds, size distributions, habit type, and degree of riming, using the ground instruments at SBU (see Table 3). The Penn State WRF ensemble Kalman filter (EnKF) modeling and data assimilation system (e.g., Zhang et al. 2009; Zhang et al. 2019) will be used to assimilate conventional observations, satellite observations, and IMPACTS airborne observations (both remotely sensed and in situ meteorological variables) to produce high-resolution 4D integrated analyses of storms. These analyses synthesize the observations across multiple observing platforms, and are being used to investigate the structure and evolution of multiscale bands and their associated dynamical, thermodynamical, and microphysical processes. The ensemble data assimilation system will also be used for targeted parameter estimation studies (e.g., Nystrom et al. 2021), which will quantify the optimum values for snow growth parameters in the bulk microphysics schemes, as well as quantify their uncertainty, with the rich in situ microphysics probe data used for evaluation. In addition to advancing

Table 3. Ground observations and instruments used during the 2020 IMPACTS deployment.

Instrument—PI/organization	Location	Geophysical quantities measured	Measurement details	Reference
Mobile rawinsondes—Lead by UIUC and SBU	Various locations in New York, New England, and Illinois	*P*, *T*, wind direction, wind speed, Td		See McMurdie et al. (2019) for instrument dataset
Fixed NOAA rawinsondes—J. Walstreicher (lead)/NWS	Fixed NWS sounding locations	*P*, *T*, wind direction, wind speed, Td		See McMurdie et al. (2019) for instrument dataset
Parsivel—P. Kollias/SBU	SBU/mobile truck	Particle size distribution, particle fall speed	Optical disdrometer	Friedrich et al. (2013)
Pluvio2—P. Kollias/SBU	SBU	Precipitation amount	Weighing gauge 1-min frequency	See McMurdie et al. (2019) for instrument dataset
MRRPro—P. Kollias/SBU	SBU/mobile truck	Precipitation intensity, fall speed and vertical air motion	K-band profiling radar (4-s, 60-m resolutions)	Maahn and Kollias (2012), Oue et al. (2021)
Ceilometers—P. Kollias/SBU	SBU/mobile truck	Cloud location	Profiling lidar backscatter 15-s, 10–60-m resolution	See McMurdie et al. (2019) for instrument dataset
KASPR—P. Kollias/SBU	SBU	Precipitation intensity, particle fall speed, wind, and vertical air motion, precipitation particle shape	VPT, PPI, and RHI measurements by Ka-band scanning polarimetric radar at high temporal and spatial resolutions	Kollias et al. (2020)
ROGER—P. Kollias/SBU	SBU	Precipitation intensity, particle fall speed and vertical air motion	W-band profiling radar, 4-s and 30-m resolutions	Lamer et al. (2021)
MWR—P. Kollias/SBU	SBU	Liquid water path	Microwave radiometer	See McMurdie et al. (2019) for instrument dataset
SKYLER—P. Kollias/SBU	SBU/mobile truck	Precipitation intensity, precipitation particle fall speed and vertical air motion, precipitation particle shape	X-band phased array radar	Kollias et al. (2020)
WFF D3R, PIP, MRR, Pluvio, Parsivel—Wolff/WFF	Wallops, Virginia	Reflectivity, Doppler velocity, and polarimetric information	Scanning Ku- and Ka-band radar	Kumar et al. (2018)
New York State Mesonet—J. Brotzge/SUNY Albany	New York State various locations	Surface meteorology and SWE, profiles of *T*, *V*, rh, liquid water	Surface observations 1-min frequency, profiling stations	Brotzge et al. (2020)

the science investigations of IMPACTS, simulations and analyses can provide insights for optimal design of data assimilation, modeling, and ensemble prediction systems for these impactful winter storms.

Successful project coordination: The 2020 deployment year

IMPACTS operations require careful coordination between forecasting, air traffic control (ATC), decision-making, aircraft flight tracks, and scheduling of ground assets. The 2020 deployment year successfully executed this coordination. When a storm of interest was forecast, the IMPACTS mission scientists designed flight tracks for the P-3 and ER-2 aircraft that were submitted 48 h in advance to the ATC agencies overseeing the airspace of interest for approval. The IMPACTS team coordinated with the NWS to discuss the forecast situation and schedule additional sounding launches (usually at 3-hourly intervals) at operational sites bracketing the planned flight time periods, and the mobile IMPACTS sounding teams were deployed to locations pertinent to the planned event. In addition, the NWS requested a *GOES-16* mesoscale sector for the time period and geographical region of interest to obtain high spatial and 1-min temporal resolution *GOES-16* imagery over the developing storm. If the storm of interest was in the vicinity of the Stony Brook radar site, the radars operated during the storm bracketing the planned flight period, with the mobile SKYLER radar positioned strategically at one of the preplanned sites on Long Island. During flight operations, adjustments to the planned flight legs were made in coordination with ATC in real time as warranted based on the observed temperature profiles and observed satellite and radar features to meet the IMPACTS science goals.

The 2020 IMPACTS deployment occurred from 10 January to 29 February 2020. A field catalog where all quick-look imagery of the data collected, science and mission reports for all flights, supporting meteorological maps, and tools for exploring each event is available at http://catalog.eol.ucar.edu/impacts_2020. The quality-controlled data for the 2020 deployment can be obtained from the Global Hydrometeorology Resource Center site for IMPACTS (McMurdie et al. 2019).

The 2020 deployment year was uncharacteristically warm along the eastern seaboard and the number of snow events was lower than typical for the region (NCEI 2020). Ten storms were sampled by aircraft (Table 4) that included two Midwest snowstorms, and a few warmer events with primarily rain at the surface. Of these storms, five storms had full coordination between the two aircraft. Figure 4 shows where the sampling took place for all the events. In the following sections, example results from the 2020 deployment highlight each of the different observing platforms and how these types of measurements address IMPACTS goals.

Preliminary results: Characterizing and understanding snowbands

Complementary measurements obtained from the ER-2 airborne radars and the P-3 in situ microphysical instruments, and how together they address the IMPACTS goals of characterizing and understanding snowbands is illustrated in Figs. 6 and 7 for the 7 February 2020 event. At this time, a rapidly deepening surface cyclone was located over eastern Pennsylvania and the aircraft made several west-to-east transects across precipitating clouds to the north over central New York State. Figure 6 relates the radar reflectivity from the 0.9° elevation angle scan of the KENX WSR-88D radar in Albany, New York, to the ER-2 X-Band Radar (EXRAD) nadir-pointing radar reflectivity cross section as the aircraft transected overhead. Although

Table 4. Description of the storms sampled during the 2020 IMPACTS deployment.

Date	Aircraft	Event description
18 Jan	P-3	Snowbands in prefrontal sector of mature cyclone over upstate New York
25 Jan	P-3, ER-2	Warm occluded front with generating cells
1 Feb	P-3, ER-2	Warm oceanic frontal system over southern Atlantic with GPM overpass
5 Feb	P-3, ER-2	Shallow frontal zone over Midwest with snowbands
7 Feb	P-3, ER-2	Heavy snow and multiple bands in a rapidly deepening cyclone over New England and New York
13 Feb	P-3	Warm front overrunning precipitation with multiple wave structures
18 Feb	P-3	Moisture overrunning a warm front with snow over Vermont and Maine
20 Feb	P-3	Coastal cyclogenesis with snowbands across North Carolina
25 Feb	P-3, ER-2	Generating cells with supercooled water in a northwest sector of a Midwest storm
27 Feb	ER-2	Snowbands wrap around a deep occluded cyclone over northern New York

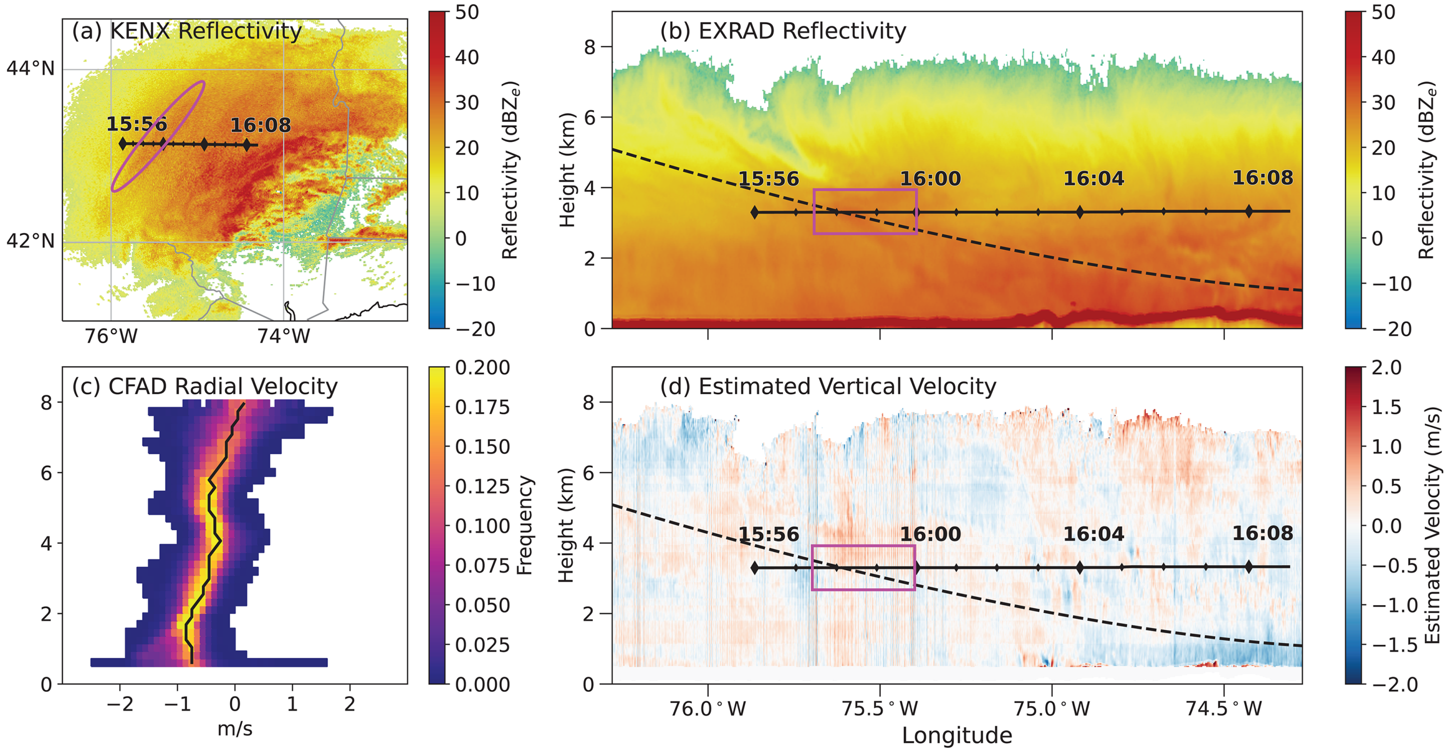

Fig. 6. Comparison of radar reflectivity (dB*Z*) from the NWS WSR-88D radar and the ER-2 radars for the 7 Feb 2020 event: (a) Albany (KENX) reflectivity from a PPI scan at 0.9° taken at 1603 UTC, (b) EXRAD reflectivity (dB*Z*), (c) contoured frequency by altitude diagram of the radial velocity measured by the HIWRAP Ka-band radar with the median drawn as a black line, and (d) estimated vertical velocity (m s^{-1}) calculated by adding the median radial velocity at each altitude as shown in (c) to the nadir pointing beam of the HIWRAP Ka-band radial velocity. The location and times of the P-3 flight leg are shown by the horizontal black line in (a), (b), and (d) and the height of the KENX scan is indicated by the dashed curved line in (b) and (d). Feature of interest discussed in text is indicated with magenta boxes or ellipse. The dark red thick line at the bottom of the panel in (b) is the ground.

the region of highest reflectivity (greater than 40 dB*Z* at ~43°N, 74.5°W) shown in Fig. 6a is associated with the bright band (where melting snow produces high reflectivity), snow was falling at the surface to the region west of 74.5°W, as measured by the New York Mesonet stations (Fig. 8).

The WSR-88D radar beam intersected the P-3 flight track at 1558 UTC and both the EXRAD and WSR-88D indicated an area of enhanced reflectivity of ~28 dB*Z* (magenta box in Fig. 6b) that is part of a snowband-like structure circled in magenta in Fig. 6a. To examine whether processes such as locally stronger upward vertical velocity is contributing to this snowband-like structure, a contoured frequency by altitude diagram (CFAD; Yuter and Houze 1995) of radial velocity measurements from the nadir pointing radars on the ER-2 (e.g., HIWRAP Ka-band radar, Fig. 6c) is used to estimate the magnitude of the vertical motion. The black contour in Fig. 6c is the median radial velocity at each altitude bin and represents the particle ensemble fall speed profile that is added to the measured HIWRAP Ka-band radial velocity to obtain an estimate of the vertical velocity following Rosenow et al. (2014). The resulting estimated vertical motion field shows that the region of interest of enhanced reflectivity at 1558 UTC near 75.5°W was also associated with a local region of upward vertical motion ~0.5 m s^{-1} (magenta box Fig. 6d).

The reflectivity profile measured by the other ER-2 radars (W, Ka, and Ku band) along with microphysical properties measured by the P-3 focusing on the same region of the snowband-like structure discussed above is shown in Fig. 7. The dual-frequency ratio, defined as the ratio of radar reflectivity factor between two wavelengths ($DFR_{Ku\text{-}Ka}$), is plotted in the bottom panel of Fig. 7a. Past studies have shown that spatial variability in

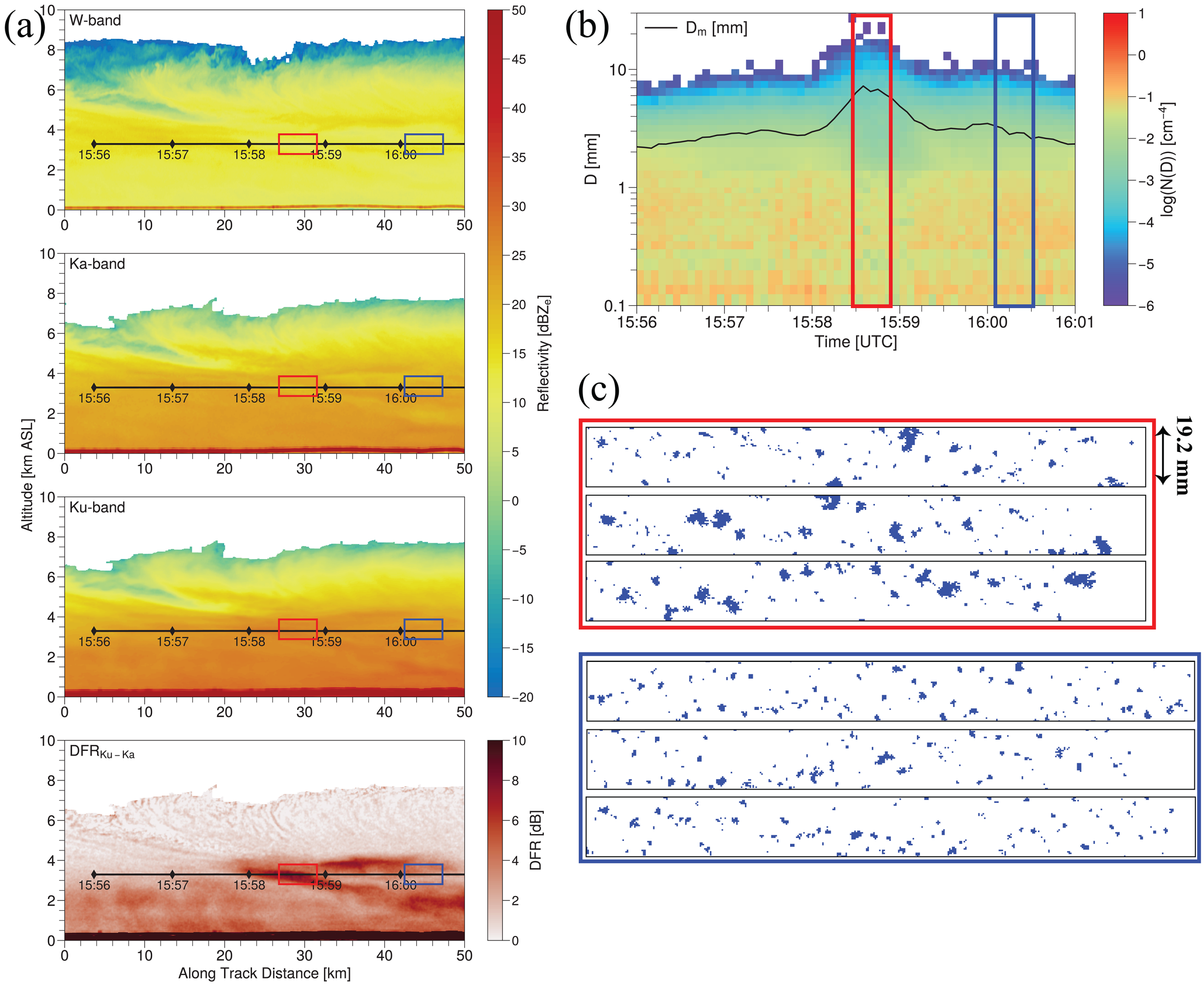

Fig. 7. Comparison of cross sections of radar reflectivity from the ER-2 radars and microphysical measurements from the P-3. (a) Radar reflectivity from the W-, Ku-, and Ka-band wavelengths of the ER-2 radars and the dual-frequency ratio between the Ku and Ka bands in the bottom panel. (b) Particle size distribution (shaded) and mass-weighted mean diameter D_m (black line). (c) Ten-second particle imagery strips from the HVPS on the P-3. The red boxes indicate a time of relative enhanced reflectivity for all radars and enhanced DFR, and the blue boxes indicate a time outside of this enhancement.

DFR is influenced by variations in microphysical properties (e.g., Matrosov et al. 2005; Liao et al. 2016; Mason et al. 2019), and the coordinated flight legs between the ER-2 and P-3 performed in IMPACTS allows further exploration of the microphysical properties that cause variations in DFR in winter cyclones. The region of enhanced DFR coincides with an increase in the mean diameter of the sampled particles (i.e., larger mass-weighted mean particle diameter D_m; Fig. 7b) and an increased number of larger particles per unit volume (highlighted with red boxes in Fig. 7) compared to the other times. Figure 7c illustrates that a significant number of large aggregates were sampled during that time. Later near 1600 UTC (blue boxes in Fig. 7), the reflectivity at all radar wavelengths was lower than before, the D_m decreased, the concentration of larger particles decreased, and aggregation was less prevalent. Additional particle imagery obtained from the PHIPS instrument from this case during other flight legs is highlighted in the "Challenges to remote sensing retrievals" sidebar.

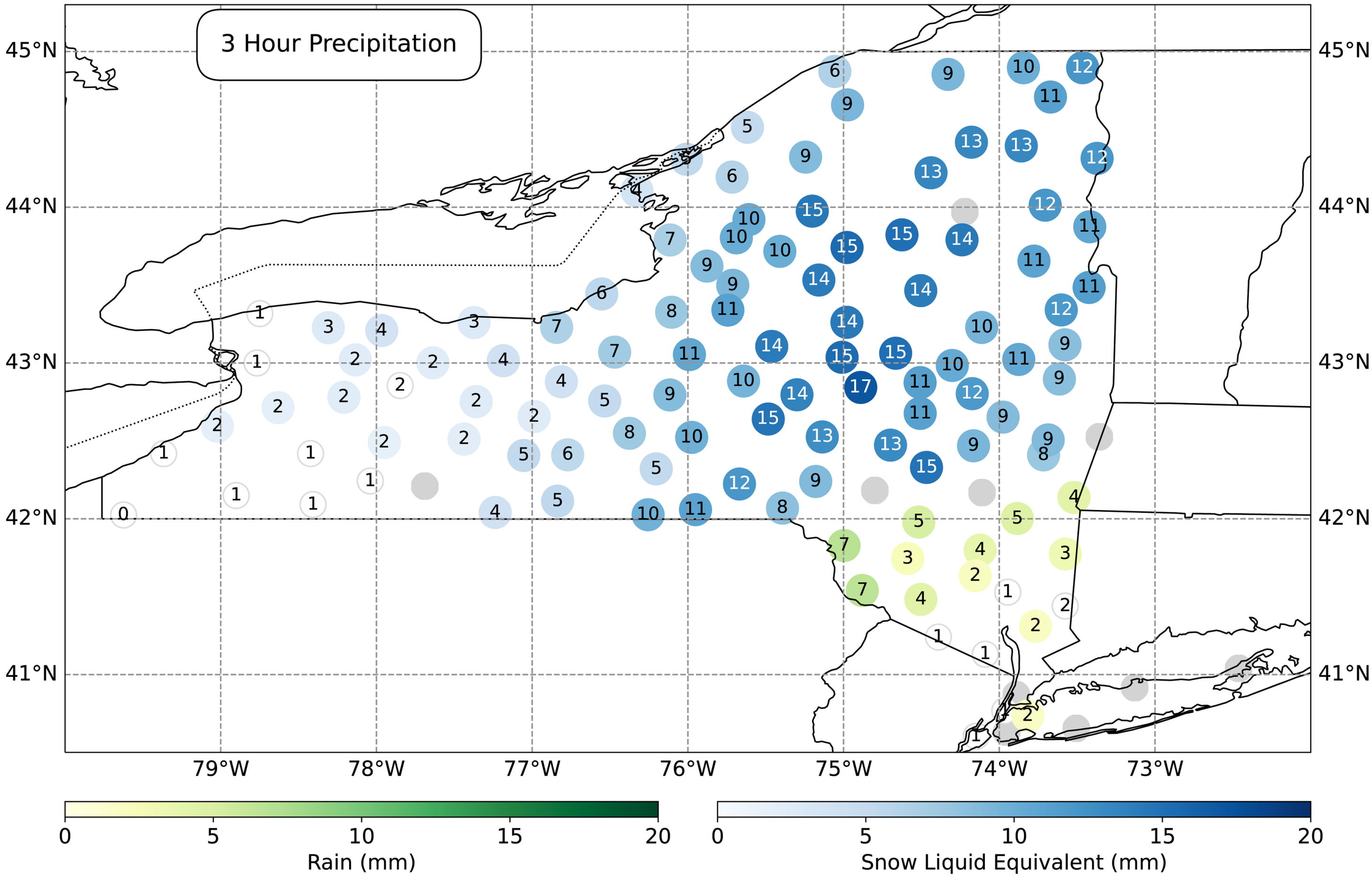

Fig. 8. **Three-hour precipitation totals (mm) from 1500 to 1800 UTC 7 Feb 2020 as measured at New York State Mesonet stations. Blue circles indicate stations where precipitation fell as snow and green circles where precipitation fell as rain.**

In this one example flight leg of the 7 February 2020 event, the snowband-like structure was characterized by locally enhanced reflectivity in the NEXRAD and ER-2 radars (magenta and red boxes in Figs. 6 and 7) and upward vertical motion which may have contributed to the increased aggregation and larger particle sizes as measured by the P-3. This example illustrates how measurements from multifrequency radars and in situ microphysics measurements together reveal processes present in snowbands. More in depth analysis of this event is ongoing addressing IMPACTS goals, such as how the vertical variability of horizontal and vertical motions translated to increased snowfall rates in central New York and how the environmental and microphysical properties varied within and outside the regions of heavier snowfall.

Another example of how the IMPACTS observations provided a synergistic view of the mesoscale processes in winter storms is illustrated with the last storm sampled during the 2020 deployment year on 27 February 2020. A mature, deep occluded cyclone was situated over northern New York, and the ER-2 sampled the region to the west of an occluded front located from Lake Ontario to Long Island. During the 0954–1005 UTC 27 February flight leg, there were wavelike features to the west of the leg evident in the 1000 UTC *GOES-16* IR imagery (Fig. 9, 43°N, 78°W). The ER-2 sampled the region immediately west of the occluded front in the cold sector and also along a convergence zone on the western edge of an 850-hPa jet situated over northeastern New York State (not shown). Variability in cloud top height or wavelike features are not obviously present along this flight track in the *GOES-16* imagery (Fig. 9). However, the 1,064-nm total attenuated backscatter from the Cloud Physics Lidar (CPL; McGill et al. 2002) and the W-band (94-GHz) CRS radar reflectivity data from the ER-2 tell a different story (Figs. 10a,b). Both CPL and CRS serve complimentary roles in IMPACTS

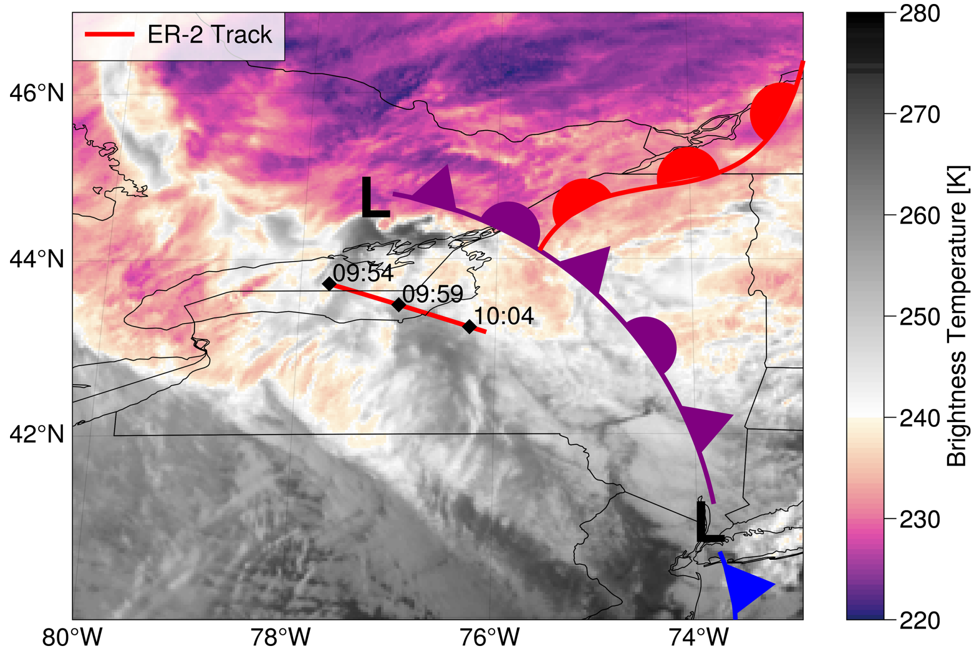

Fig. 9. Infrared brightness temperatures from the Advanced Baseline Imager channel 13 of *GOES-16* (color shades) at 1000 UTC 27 Feb 2020 with the ER-2 flight track as a red line with times overlaid. The overlaid frontal analysis with standard frontal symbols is valid 1000 UTC and is based on interpolating the 0900 and 1200 UTC 27 Feb 2020 National Weather Service Weather Prediction Center surface analyses.

due to their respective strengths and weaknesses. CPL can measure optically thin cloud tops and nonprecipitating cloud particles below CRS's minimum detection threshold (−28 dB*Z*), whereas CRS provides extensive hydrometer particle information below where CPL fully attenuates (cloud optical depth of ~3.0). CRS shows the nearly ubiquitous presence of tilted fall streaks of varying intensity throughout the flight line. Model and rawinsonde data (not shown) indicate enhanced speed and direction shear, especially in regions where the tilted fall streaks are most pronounced (~3–4 km above sea level, ~0956 UTC), which is near and just above the height of the frontal inversion. Despite these insights from CRS, its lower sensitivity limits its application near cloud top where CPL detected an extensive layer of optically thin clouds. Thus, CRS echo tops heights were up to 1 km lower than detected by CPL (~0955 UTC).

CPL and CRS data limitations however motivate both this and previous studies (i.e., McGill et al. 2004; Delanoë and Hogan 2010; Mace and Zhang 2014) to develop combined lidar–radar data products to provide a holistic view of the hydrometer and storm vertical structure. The combined CRS–CPL data product shown in Fig. 10c shows the maximum normalized signal (CRS = reflectivity, CPL = backscatter) derived from both data products. Normalization was achieved by differencing all grid points from their dataset minimum and then dividing this difference by an empirically derived range of values observed for each instrument during the IMPACTS 2020 field campaign. In Fig. 10c, values range between 0 (weak return signal) and 1 (strong return signal) with regions of overlap denoted with stippling. These data show that the wavelike or fall streak pattern evident in CRS data were most likely obscured from *GOES-16* (Fig. 9) due to optical thin clouds farther aloft and also affords a more comprehensive visualization of the fall streaks than either CPL or CRS could provide independently. Additionally, IMPACTS affords the unique opportunity to develop and test combined lidar (Yorks et al. 2011; Midzak et al. 2020) and radar (Oue et al. 2015) data products to enable pseudomicrophysical retrievals. Such retrievals would provide information about particle shape and phase from cloud top to the surface, which can be evaluated with the IMPACTS suite of in situ cloud particle measurements. Preliminary results using normalized combined CRS–CPL depolarization data (not shown) suggest that particle phase changes often mirrored the wavelike patterns seen in Fig. 10c. Visualizing and analyzing both storm structure and its underlying microphysical characteristics via merged data products, in the context of model, space, and airborne data, affords the unique opportunity to investigate how these wavelike patterns form, their microphysical characteristics, and their potential role in forming and maintaining snowbands.

Research quality ground-based radars installed at SBU (Table 3) are critical for characterizing the short time-scale evolution of snowband structures and associated mechanisms contributing to snowband maintenance which cannot be addressed by the aircraft sampling. Figure 11 highlights the ground observations made as a warm frontal snowband located in the pre-frontal sector north of the surface warm front crossed over Long Island and southern New England on 18–19 January 2020. The WSR-88D KOKX radar observed a north-northwest–south-southeast oriented primary snowband passing through SBU near 1900 UTC 18 January 2020 (Fig. 11a). The SBU radars allow the exploration of snowband mechanisms for this event. Vertical and quasi-vertical profiles (Ryzhkov et al. 2016; Kumjian and Lombardo 2017) from radars at SBU all show a rapid onset of snowfall to the surface around this time, as the dry low-level air ahead of the band retreated (Figs. 11b–d). There were fall streaks from convective cells aloft that had higher reflectivities toward the ground in the W-band (ROGER) and MRR reflectivity fields (Figs. 11b,d), but the band was also located within a layer of frontogenesis from 900 to 850 hPa and associated with upward motion (not shown).

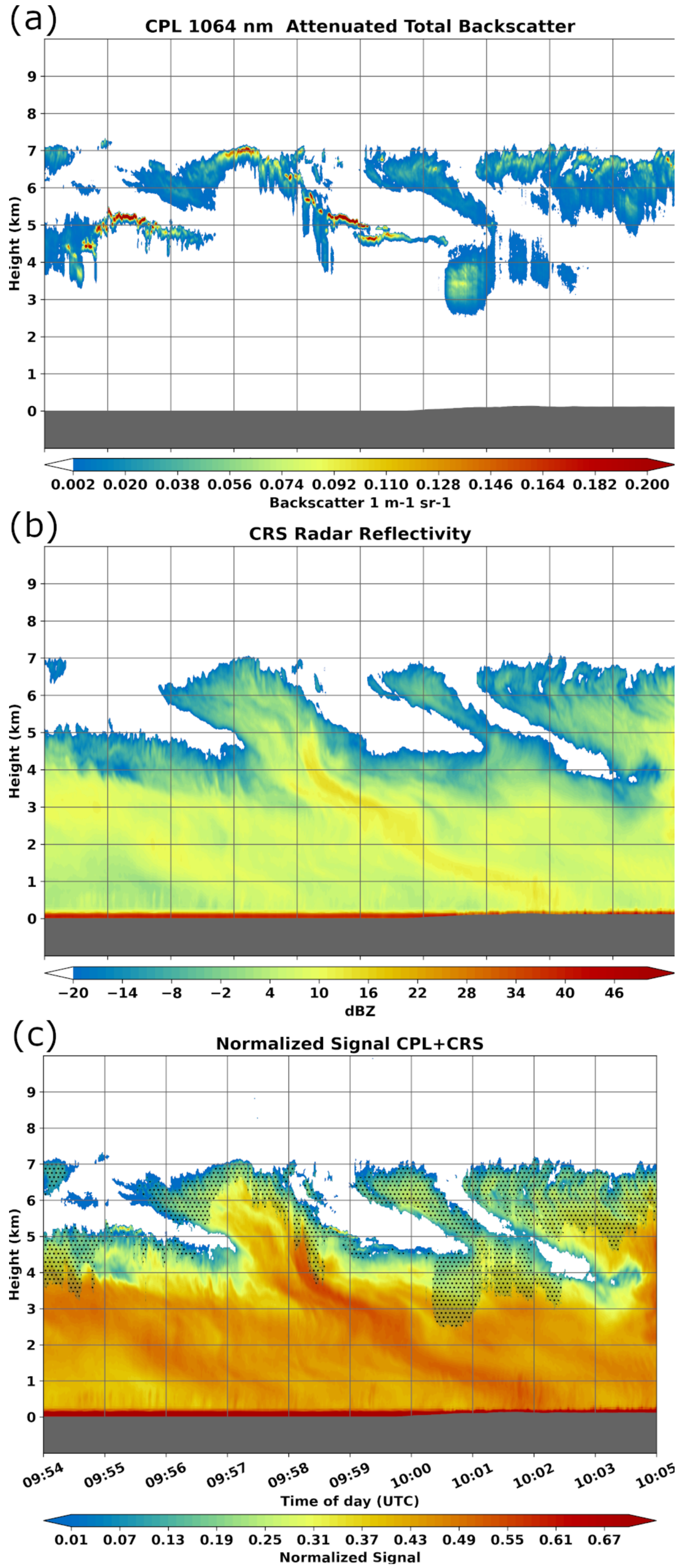

Fig. 10. CPL and CRS and combined CPL–CRS signal from the 0954–1005 UTC 27 Feb 2020 ER-2 flight leg. (a) Attenuated total backscatter from the CPL, (b) CRS reflectivity, and (c) normalized signal from the CPL and CRS where stippling indicates overlap between the two instruments.

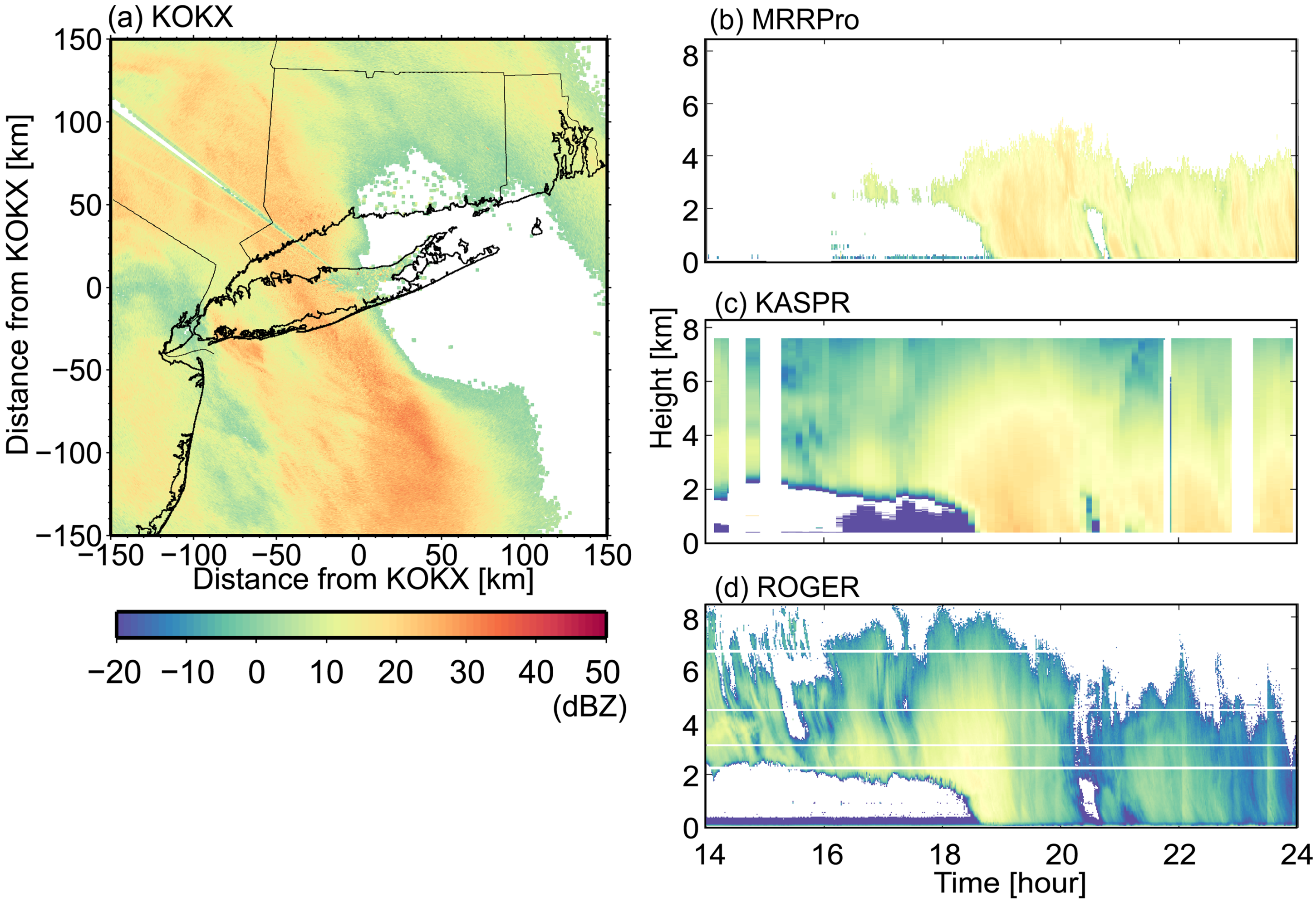

Fig. 11. Radar sampling of the 18 Jan 2020 event from the Stony Brook radar site. (a) Radar reflectivity from the KOKX WSR-88D radar on Long Island at the 0.5° elevation angle at 1904 UTC, and height–time cross sections of (b) MRRPro reflectivity at Cedar Beach, (c) quasi-vertical pointing KASPR reflectivity at SBU, and (d) ROGER (W-band) reflectivity from 1400 to 2359 UTC.

The KASPR radar has fully polarimetric capabilities and operated in range–height indicator mode, sampling across the band as it moved across Long Island. Movies of reflectivity, spectrum width and specific differential phase (K_{DP}) from the KASPR radar for more than a 2-h period as the band moved across Long Island are provided as supplemental material (https://doi.org/10.1175/BAMS-D-20-0246.2). Multiple layers of turbulence below 4 km AGL were inferred from the spectrum width measurements as the band moved across Long Island. These turbulent motions could have provided a mechanism for aggregation and additional particle mass growth by riming. Multiscale processes such as vertical motions associated with frontogenesis and turbulent motions all appear to have contributed to the snowfall mechanisms associated with this case. Ongoing analysis of this event and others where the ground-based radar observations can be related to the airborne remote sensing and in situ observations will provide considerable insights to the processes contributing to banded structures.

Preliminary results: Applying IMPACTS observations to remote sensing of precipitation

The IMPACTS observational strategy of coincident remote sensing and in situ microphysical measurements in precipitating winter cyclones is especially beneficial when they align along a GPM satellite overpass, such as the 1 February 2020 event when the aircraft lined up under a 1435 UTC GPM overpass over the Atlantic Ocean. Figure 12 shows the visible satellite image of the cloud field associated with a developing surface low off the North Carolina coast on

1 February 2020 with the GPM overpass and the ER-2 flight track overlaid. Although this event was warm and produced rain at the surface, the measurements obtained by IMPACTS address the science goal to improve remote sensing of precipitation. The ER-2 flew over several fine-scale west–east oriented linear bands of thicker clouds between 36° and 37°N. The reflectivity field from the HIWRAP Ku-band radar in Fig. 13a illustrates that these bands were tall convective turrets extending to over 8 km above sea level, about 3 km above the top of the broader cloud deck. The reflectivity was also enhanced along the bright band under these turrets (especially at 35.9°, 36.4°, and 37.2°N) compared to other locations, and there appears to be heavy precipitation reaching the surface beneath these regions. The GPM DPR Ku-band reflectivity plotted in Fig. 13b also confirms the presence of narrow and tall convective turrets and enhanced reflectivity at the bright band and below at the same locations listed above. The DPR has coarser resolution than HIWRAP and shows evidence of significant nonuniform beam filling. The P-3 flew underneath the ER-2 at 5-km elevation and sampled the tops of the lower cloud deck and within the convective turrets. Figure SB2 in the "Challenges to remote sensing retrievals" sidebar shows some sample particle imagery from the PHIPS and CPI during this transect. When the P-3 was sampling the top of the lower cloud deck (~36.125°N in Fig. 13), the temperature was −10°C and all the particles were supercooled liquid drops (see first image in Fig. SB2). Then when the P-3 entered the convective turret at 36.25°N, the cloud particles were predominantly ice and included capped columns and plate aggregates (see imagery highlighted within the purple box in Fig. SB2). This example shows the rich variations in the precipitation structures detected from the airborne instrumentation that can then be applied to the evaluation and future development of satellite retrievals of microphysical properties and rain rate.

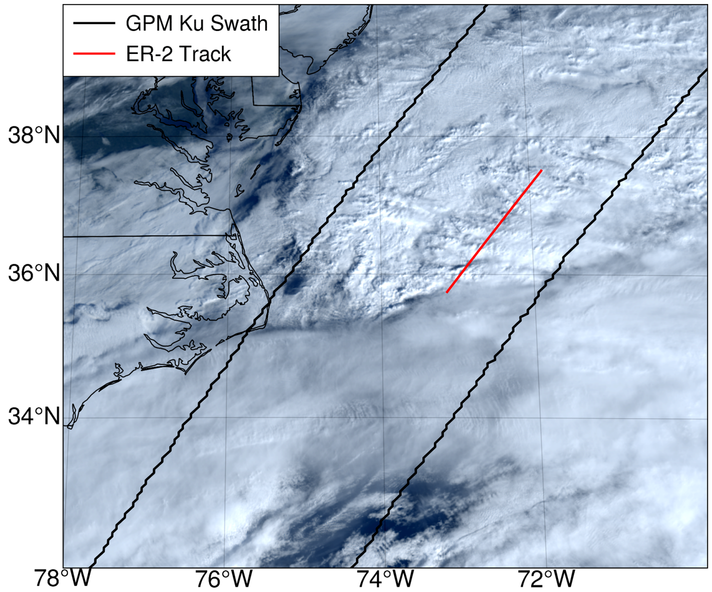

Fig. 12. Visible imagery from the *GOES-16* satellite for 1440 UTC 1 Feb 2020 during the time of the GPM overpass. The GPM Ku-band swath is shown with black lines, and the coincident track of the ER-2 aircraft is shown with a red line.

The ER-2 also flew two microwave radiometers, AMPR and CoSMIR (Table 1). AMPR's frequencies make up much of the lower end of the GMI, whereas the CoSMIR frequencies span the upper end of GMI and include frequencies that are sensitive to both rain and snowfall. This airborne passive-microwave observing suite's role in IMPACTS is to characterize the horizontal structure of precipitation systems, and to enable combined active-passive retrievals of rain and snowfall similar to the GPM combined algorithm and related approaches (Grecu et al. 2016; Olson et al. 2016). They are also sensitive to particle phase, size, and shape. Thus, these radiometers tie into all three IMPACTS goals: characterize spatial/temporal scales of heavy winter precipitation, understand processes occurring in heavy winter precipitation, and apply this information to improving remote sensing of precipitation.

Figure 14 shows AMPR, CoSMIR, and GMI swaths that observed precipitation during the same GPM overpass illustrated in Fig. 13. The southern portion of the leg overflew strong convection (near 36°N, 73°W), where high brightness temperatures (~250 K) at 10.7 GHz (Fig. 14a) indicate heavy rain. This high brightness temperature (Tb) at 35.9°N corresponds to the leftmost convective turret in Figs. 13a and 13b discussed above. In this same region, the 37.1- and 85.5-GHz channels (Figs. 14c,d) showed brightness temperature minima located within broader areas of warm temperatures, the latter associated with emission from liquid cloud and rain (Weinman and Guetter 1977). Local minima of brightness temperatures in these channels are due to scattering of the upwelling radiation by the presence of ice, which was confirmed by the P-3 PHIPS measurements (Fig. SB2). The CoSMIR 165.5 and 183.31 ± 7 GHz Tb values were depressed in this region as well (Figs. 14e,f), confirming strong scattering by ice, and that ice processes within the cloud contributed to heavy precipitation (a simple reflectivity-rainfall relationship applied to EXRAD observations suggested rain rates in excess of 50 mm h^{-1} in this core).

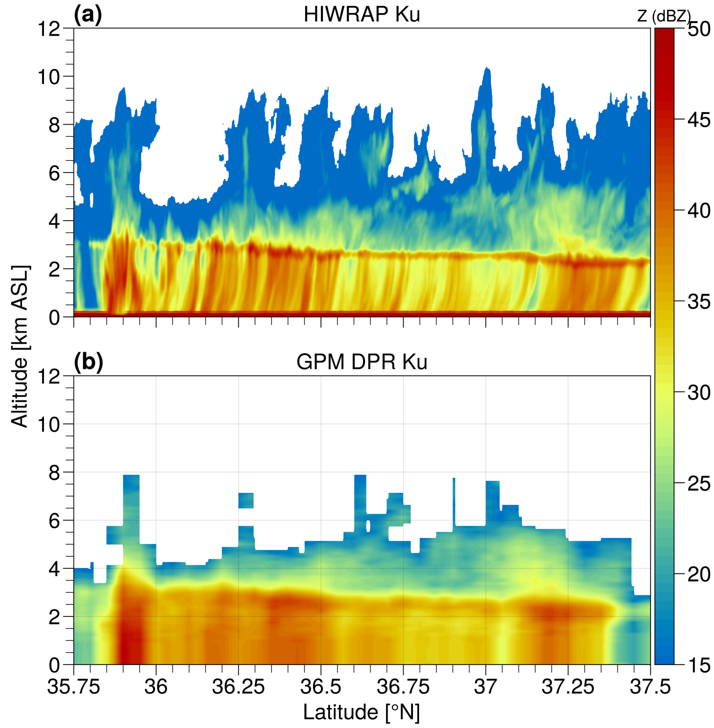

Fig. 13. Comparison of the (a) HIWRAP and (b) GPM DPR Ku-band reflectivity (dB*Z*) during the GPM overpass at 1435 UTC 1 Feb 2020.

The polarization difference (PD), defined as the difference between the vertical- and horizontal-polarized Tb values for CoSMIR 165.5 GHz and the GMI at 166 GHz are shown in Figs. 14g and 14h. The CoSMIR and GMI PDs agree well with minor differences due to instrument characteristics. The CoSMIR 165.5-GHz PD field shows an even more striking correspondence to the convective bands evident in the *GOES-16* visible imagery and the HIWRAP reflectivity (Figs. 12, 13, and 14g). Gong and Wu (2017) and Gong et al. (2020) demonstrated that PD values tend to be higher (>5 K) in stratiform and anvil cloud regions due to the prevalence of predominantly horizontally oriented ice. This effect was observed in the weaker precipitation north of 36°N. Within the convection near 36°N, PD values were somewhat less (by 1–2 K), especially in the GMI observations (Fig. 14h). This suggested more randomized ice particle orientations likely associated with the deep convection there (Fig. SB2; Gong et al. 2020).

The ice scattering signatures seen in both the AMPR and CoSMIR fields at 37.1 GHz and higher frequencies and the presence of ice particles confirmed by the P-3 PHIPS instrument (Fig. SB2) indicated that the presence of larger and/or higher concentrations of ice particles played a significant role in the overall precipitation formation for this event, particularly for the heaviest precipitation cores.

Looking forward to the next deployments

IMPACTS successfully measured precipitation structures in 10 winter cyclone events in 2020. Preliminary results highlighted here point to the roles of locally enhanced upward vertical motion, aggregation, wave activity and elevated convection in the observed snowband structures in different storms. In-depth analysis of these cases is ongoing (e.g., Chase et al. 2022, manuscript submitted to *J. Appl. Meteor. Climatol.*; Heymsfield et al. 2021; Schultz et al. 2021; Dunnavan et al. 2022, manuscript submitted to *J. Appl. Meteor. Climatol.*; Finlon et al. 2022, manuscript submitted to *J. Atmos. Sci.*), focusing on the dynamical and thermodynamical processes, and microphysical structures occurring within and outside of snowbands. With the success of the 2020 deployment, the IMPACTS team looks forward to two more winter seasons of measurements,

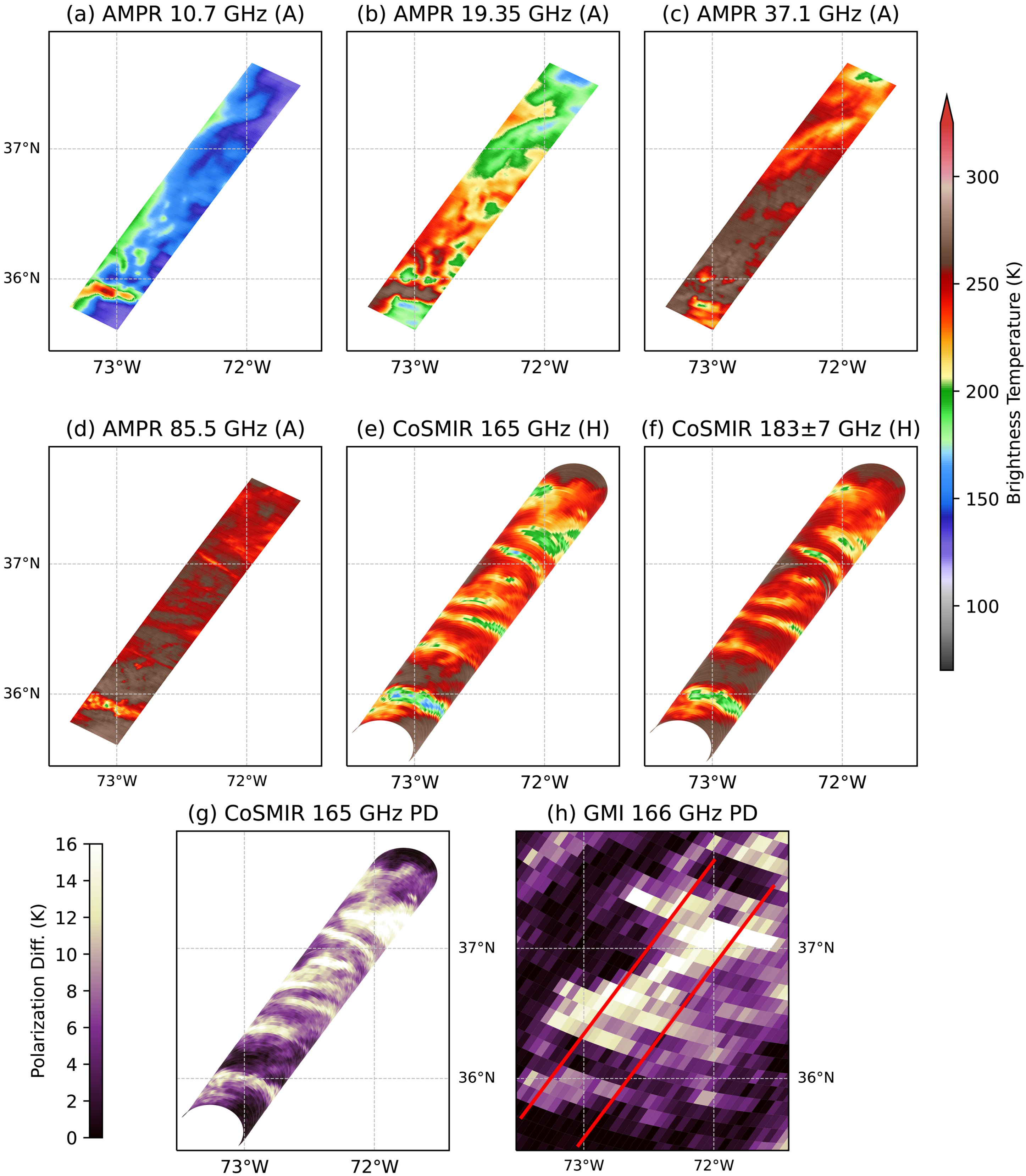

Fig. 14. AMPR brightness temperatures coinciding with the GPM overpass at 1435 UTC 1 Feb 2020 at (a) 10.7, (b) 19.35, (c) 37.1, and (d) 85.5 GHz. CoSMIR brightness temperatures at (e) 165 and (f) 183 ± 7 GHz. (g) CoSMIR and (h) GMI polarization differences for the 165-GHz channels are shown. Red lines in (h) indicate the scan width of the CoSMIR radiometer. Longitude (*x* axis) and latitude (*y* axis) grid lines are shown.

currently planned for January–February 2022 and January–February 2023. The two aircraft will carry essentially the same instrument packages as the first deployment with a full set of microphysical probes on the P-3 and active and passive remote sensing instruments on the ER-2.

The ground component will remain primarily focused on Long Island, with extensive instrumentation installed there. The SKYLER mobile X-band radar will have the ability to travel in an approximate 300-km radius from Stony Brook enabling the IMPACTS team to strategically deploy this radar and the mobile sounding unit in a broader region for storm systems of interest. An example of the unique ability of the SKYLER radar to sample detailed precipitation structure through high temporal scanning is shown as a movie in the supplemental material. The IMPACTS team is also interested in collaborating with other research groups to expand the ground component of the observing network, especially those with ground-based instrumentation suited for measuring winter cyclones in the Northeast or Midwest regions of the United States. Please contact the authors if interested in participating in the IMPACTS 2023 deployment. As the IMPACTS project moves forward, the in situ and remote sensing measurements of precipitation structures and processes will ultimately address long-standing questions regarding processes contributing to the initiation, structure, and evolution of snowbands in winter cyclones, improve snowfall retrievals from space-based missions such as GPM, and improve numerical weather prediction model forecasts of snowfall during U.S. snowstorms.

Early career and student participation

The IMPACTS project puts a high priority on training the next generation of science leaders by empowering students and early-career professionals to perform critical mission support roles and participate in data collection efforts. Thus, students and early career scientists are key to the success of IMPACTS mission operations and science analysis. Without their expertise, hard work, and enthusiasm, IMPACTS would not be possible. These individuals performed multiple roles during the IMPACTS 2020 deployment, such as 1) performing sounding observations in remote locations, 2) operating ground-based radar systems for coordination with aircraft measurements, and 3) providing twice daily forecast briefings to the entire IMPACTS team. Students and early career scientists also served as members of the ER-2 instrument teams, while others served as onboard P-3 mission scientists and P-3 instrument operators, communicating in real time with the operations center during flights. Several of these individuals also had leadership roles in the operations center as the lead mission scientists, where they communicated decisions regarding flight tracks to the flight coordinators in real time and enabled each flight mission to achieve the science goals. Examples of the participation by these individuals are shown in Fig. SB1.

Fig. SB1. Photos from the field. (a) Students launching balloon soundings on Long Island; (b) forecasters A. DeLaFrance (left), C. Helms (center), and S. Nicholls (right) preparing a briefing; (c) V. McDonald preparing to board the P-3 for a science flight; (d) G. Sova (left) and K. Sand (right) with PHIPS instrument PI, M. Schnaiter (center), on the P-3 between flights. Photo credits: (a) B. Colle, (b),(d) V. Salazar, (c) V. McDonald taken by J. Finlon.

Challenges to remote sensing retrievals

There are many challenges to remote sensing retrievals of ice-phase precipitation within winter extratropical cyclones. Radar and passive microwave measurements from spaceborne instruments are strongly affected by particle geometry, which includes not only the size–density spectrum of particles, but also the relative concentrations of pristine and aggregate crystals, the aspect ratios and canting angles of the particles, and their degree of riming. To address these uncertainties, IMPACTS measurement strategy includes in situ

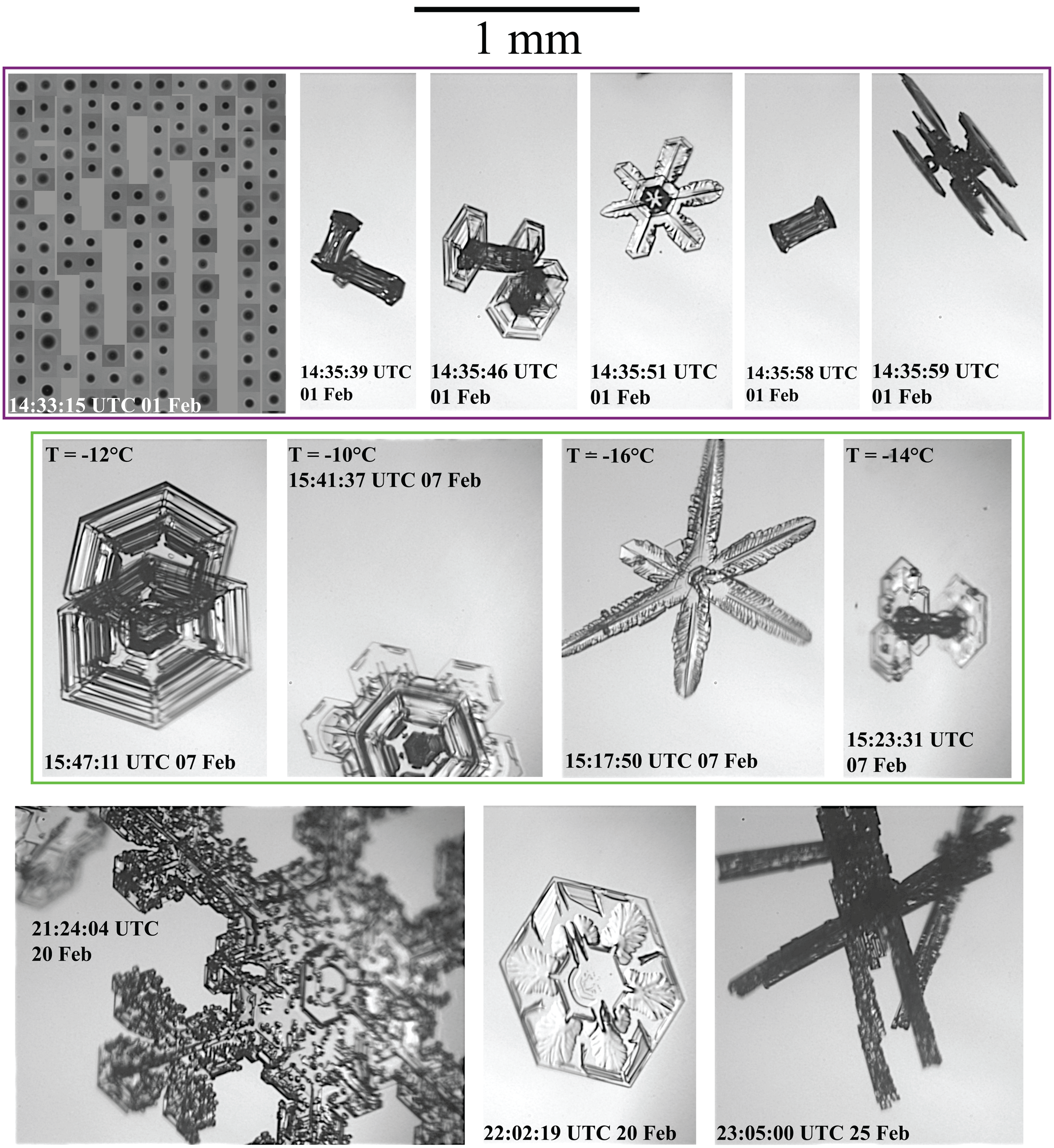

Fig. SB2. Sample particle images taken by the PHIPS and CPI instruments on the P-3 during IMPACTS 2020. Times and dates for each image are shown. The images grouped in the purple box are from the 1 Feb case and the images grouped in the green box are from the 7 Feb case arranged so that the images on the left side were from the western portions of the flight legs and the images on the right side were from the eastern portions of the flight legs.

measurements from the P-3 of particle geometries/habits and intrinsic bulk microphysical properties (e.g., ice water content, cloud liquid water, supercooled water content) as well as active and passive remote sensing measurements from the ER-2. Examples of the range of particle types measured during the IMPACTS 2020 deployment as sampled by the PHIPS and CPI instruments are shown in Fig. SB2. The top group of images within the purple box were all collected during the 1 February 2020 event highlighted in Figs. 13 and 14. The first image of supercooled liquid water droplets is from the CPI instrument collected when the P-3 was skimming the tops of the clouds at 5 km. The rest in this box were collected when the P-3 entered a convective turret and the particles rapidly transitioned to primarily ice of mostly capped columns and plate aggregates. The middle group of images within the green box were all collected during the 7 February 2020 event highlighted in Figs. 6 and 7. They are arranged so that the leftmost image was collected from the westmost portion of the flight leg and the rightmost image was from the eastern portion of the storm sampled by the P-3. They were collected at different temperatures as shown on the figure. These examples are only a small fraction of the range particles sampled during IMPACTS. These measurements will contribute to improving and constraining current and future retrieval algorithms of ice-phase precipitation.

Acknowledgments. This article is dedicated to Drs. Fuqing Zhang and Gail Skofronick-Jackson, whose contributions and enthusiastic support for IMPACTS and other projects have been instrumental in advancing knowledge of precipitation systems and advancing the state of spaceborne measurements of precipitation. Field campaigns of this size depend on the dedication and support of many individuals and institutions. We thank the support of the NASA Earth Science Division (ESD), Earth Venture Suborbital Program under the NASA Airborne Science Program and especially M. Martin, and J. Olsen in the Earth System Science Pathfinder Program (ESSP) that manages the Earth Venture Suborbital Program (EVS-3), B. Tagg of the ESD Airborne Science Program, and J. Kaye and B. Lefer of the ESD Research Program. The National Weather Service (NWS) provided invaluable support throughout the 2020 deployment and plan to continue their integral involvement in future deployments. We especially thank NWS's J. Waldstreicher for scheduling supplemental rawinsonde launches, *GOES-16* mesoscale sectors and for connecting our forecasting team with on-duty NWS Eastern Region and Weather Prediction Center forecasters for daily forecasting support. We thank all members of the IMPACTS instrument teams for the important contributions to the mission's success. In addition to the authors of this paper, the following people have leadership roles in IMPACTS. For overall logistics support and management: V. Salazar, Project Manager, C. Murphy and K. Stern, from the NASA ARC's Earth Science Project Office. Aircraft operations: J. Nystrom, W. Klein, B. Hobbs, F. Becker, M. Cropper, G. Everson, and K. Griffin, and the ER-2 and P-3 pilots, crew, and support teams. Aircraft instrument leads, IMPACTS coinvestigators, and mission science operations: I. Adams, D. Doleen, M. Fritts, M. Grecu, S. Guimond, L. Li, M. McGill, M. Miller, J. Munchak, D. Noone, M. Schnaiter, C. Schultz, L. Thornhill, and D. Toohey. Data management: S. Brodzik, G. Stano. Forecasting: A. DeLaFrance, M. Han, S. Harkema, C. Helms, D. Hueholt, B. Kiel, M. Leonardo, R. Patel, R. Schrom, L. Tomkins, and P. Yeh. P-3 instrument operators: A. Bansemer, K. Sand, G. Sova, C. Robinson, and F. Waitz. Rawinsonde launching teams: T. Zaremba, A. Janiszeski, the students of the UIUC Atmospheric Sciences Department, the SUNY Stony Brook Atmospheric Sciences Department, and the NCSU Sounding Club. University participants are supported for IMPACTS by NASA Grants 80NSSC19K0338 (UW), 80NSSC19K0354 (NCSU), 80NSSC19K0452 (PSU), 80NSSC19K0399 (OU), 80NSSC19K0355 (UI), 80NSSC19K0394 (SBU), 80NSSC19K0328 (UND), 80NSSC19K1612 (NCAR), 80NSSC20K1876 (NCAR), 80NSSC19K0397 (NCAR), and 80NSSC20K0729 (CU).

Data availability statement. All IMPACTS quick-look images and mission scientist reports from the 2020 deployment are highlighted in the IMPACTS field catalog at http://catalog.eol.ucar.edu/impacts_2020 and the data can be obtained from the Global Hydrology Resource Center Distributed Active Archive Center at https://ghrc.nsstc.nasa.gov/uso/ds_details/collections/impactsC.html and McMurdie et al. (2019).

References

Abdelmonem, A., E. Järvinen, D. Duft, E. Hirst, S. Vogt, T. Leisner, and M. Schnaiter, 2016: PHIPS–HALO: The airborne Particle Habit Imaging and Polar Scattering probe—Part 1: Design and operation. *Atmos. Meas. Tech.*, **9**, 3131–3144, https://doi.org/10.5194/amt-9-3131-2016.

Amiot, C. G., S. K. Biswas, T. J. Lang, and D. I. Duncan, 2021: Dual-polarization deconvolution and geophysical retrievals from the Advanced Microwave Precipitation Radiometer during OLYMPEX/RADEX. *J. Atmos. Oceanic Technol.*, **38**, 607–628, https://doi.org/10.1175/JTECH-D-19-0218.1.

Barrick, J. D. W., J. A. Ritter, C. E. Watson, M. W. Wynkoop, J. K. Quinn, and D. R. Norfolk, 1996: Calibration of the NASA turbulent air motion measurement system. NASA Tech. Paper 3610, 24 pp., https://ntrs.nasa.gov/api/citations/19970010469/downloads/19970010469.pdf.

Black, A. W., and T. L. Mote, 2015: Characteristics of winter-precipitation-related transportation fatalities in the United States. *Wea. Climate Soc.*, **7**, 133–145, https://doi.org/10.1175/WCAS-D-14-00011.1.

Bosart, L. F., and F. Sanders, 1986: Mesoscale structure in the megalopolitan snowstorm of 11–12 February 1983. Part III: A large-amplitude gravity wave. *J. Atmos. Sci.*, **43**, 924–939, https://doi.org/10.1175/1520-0469(1986)043<0924:MSITMS>2.0.CO;2.

Brotzge, J. A., and Coauthors, 2020: A technical overview of the New York State Mesonet standard network. *J. Atmos. Oceanic Technol.*, **37**, 1827–1845, https://doi.org/10.1175/JTECH-D-19-0220.1.

Chase, R. J., and Coauthors, 2018: Evaluation of triple-frequency radar retrieval of snowfall properties using coincident airborne in situ observations during OLYMPEX. *Geophys. Res. Lett.*, **45**, 5752–5760, https://doi.org/10.1029/2018GL077997.

Claffey, K. J., K. F. Jones, and C. C. Ryerson, 1995: Use and calibration of Rosemount ice detectors for meteorological research. *Atmos. Res.*, **36**, 277–286, https://doi.org/10.1016/0169-8095(94)00042-C.

Connelly, R., and B. A. Colle, 2019: Validation of snow multibands in the comma head of an extratropical cyclone using a 40-member ensemble. *Wea. Forecasting*, **34**, 1343–1363, https://doi.org/10.1175/WAF-D-18-0182.1.

Delanoë, J., and R. J. Hogan, 2010: Combined CloudSat-CALIPSO-MODIS retrievals of the properties of ice clouds. *J. Geophys. Res.*, **115**, D00H29, https://doi.org/10.1029/2009JD012346.

Ding, S., G. M. McFarquhar, S. W. Nesbitt, R. J. Chase, M. R. Poellot, and H. Wang, 2020: Dependence of mass–dimensional relationships on median mass diameter. *Atmos.*, **11**, 756, https://doi.org/10.3390/atmos11070756.

Dirks, R. A., J. P. Kuettner, and J. A. Moore, 1988: Genesis of Atlantic Lows Experiment (GALE): An overview. *Bull. Amer. Meteor. Soc.*, **69**, 148–160, https://doi.org/10.1175/1520-0477(1988)069<0148:GOALEA>2.0.CO;2.

Duffy, G., G. McFarquhar, S. W. Nesbitt, and R. Bennartz, 2021: Demonstration of a consistent relationship between dual-frequency reflectivity and the mass-weighted mean diameter in measurements of frozen precipitation from GCPEX, OLYMPEX, and MC3E. *J. Atmos. Sci.*, **78**, 2533–2547, https://doi.org/10.1175/JAS-D-20-0174.1.

Field, P. R., and Coauthors, 2017: Secondary ice production: Current state of the science and recommendations for the future. *Ice Formation and Evolution in Clouds and Precipitation: Measurement and Modeling Challenges, Meteor. Monogr.*, No. 58, Amer. Meteor. Soc., https://doi.org/10.1175/AMSMONOGRAPHS-D-16-0014.1.

Finlon, J. A., G. M. McFarquhar, S. W. Nesbitt, R. M. Rauber, H. Morrison, W. Wu, and P. Zhang, 2019: A novel approach for characterizing the variability in mass–dimension relationships: Results from MC3E. *Atmos. Chem. Phys.*, **19**, 3621–3643, https://doi.org/10.5194/acp-19-3621-2019.

Friedrich, K., S. Higgins, F. J. Masters, and C. R. Lopez, 2013: Articulating and stationary PARSIVEL disdrometer measurements in conditions with strong winds and heavy rainfall. *J. Atmos. Oceanic Technol.*, **30**, 2063–2080, https://doi.org/10.1175/JTECH-D-12-00254.1.

Ganetis, S. A., and B. A. Colle, 2015: The thermodynamic and microphysical evolution of an intense snowband during the northeast U.S. blizzard of 8–9 February 2013. *Mon. Wea. Rev.*, **143**, 4104–4125, https://doi.org/10.1175/MWR-D-14-00407.1.

——, ——, S. E. Yuter, and N. P. Hoban, 2018: Environmental conditions associated with observed snowband structures within northeast U.S. winter storms. *Mon. Wea. Rev.*, **146**, 3675–3690, https://doi.org/10.1175/MWR-D-18-0054.1.

Geerts, B., and P. V. Hobbs, 1991: Organization and structure of clouds and precipitation on the mid-Atlantic coast of the United States. Part IV: Retrieval of the thermodynamic and microphysical structures of a frontal rainband from Doppler radar data. *J. Atmos. Sci.*, **48**, 1287–1305, https://doi.org/10.1175/1520-0469(1991)048<1287:OASOCA>2.0.CO;2.

Gong, J., and D. L. Wu, 2017: Microphysical properties of frozen particles inferred from Global Precipitation Measurement (GPM) Microwave Imager (GMI) polarimetric measurements. *Atmos. Chem. Phys.*, **17**, 2741–2757, https://doi.org/10.5194/acp-17-2741-2017.

——, and Coauthors, 2020: Linkage among ice crystal microphysics, mesoscale dynamics, and cloud and precipitation structures revealed by collocated microwave radiometer and multifrequency radar observations. *Atmos. Chem. Phys.*, **20**, 12633–12653, https://doi.org/10.5194/acp-20-12633-2020.

Grecu, M., W. S. Olson, S. J. Munchak, S. Ringerud, L. Liao, Z. Haddad, B. L. Kelley, and S. F. McLaughlin, 2016: The GPM combined algorithm. *J. Atmos. Oceanic Technol.*, **33**, 2225–2245, https://doi.org/10.1175/JTECH-D-16-0019.1.

——, L. Tian, G. M. Heymsfield, A. Tokay, W. S. Olson, A. J. Heymsfield, and A. Bansemer, 2018: Nonparametric methodology to estimate precipitating ice from multiple-frequency radar reflectivity observations. *J. Appl. Meteor. Climatol.*, **57**, 2605–2622, https://doi.org/10.1175/JAMC-D-18-0036.1.

Greybush, S. J., S. Saslo, and R. Grumm, 2017: Assessing the ensemble predictability of precipitation forecasts for the January 2015 and 2016 East Coast winter storms. *Wea. Forecasting*, **32**, 1057–1078, https://doi.org/10.1175/WAF-D-16-0153.1.

Griffin, E. M., T. J. Schuur, A. V. Ryzhkov, H. D. Reeves, and J. C. Picca, 2014: A polarimetric and microphysical investigation of the Northeast blizzard of 8–9 February 2013. *Wea. Forecasting*, **29**, 1271–1294, https://doi.org/10.1175/WAF-D-14-00056.1.

Guarino, J., and T. Firestine, 2010: Effects of the February 2010 snowstorms on airline performance. U.S. Dept. of Transportation Special Rep., 5 pp., http://purl.fdlp.gov/GPO/gpo54017.

Guimond, S. R., L. Tian, G. M. Heymsfield, and S. J. Frasier, 2014: Wind retrieval algorithms for the IWRAP and HIWRAP airborne Doppler radars with applications to hurricanes. *J. Atmos. Oceanic Technol.*, **31**, 1189–1215, https://doi.org/10.1175/JTECH-D-13-00140.1.

Hadlock, R., and C. W. Kreitzberg, 1988: The Experiment on Rapidly Intensifying Cyclones over the Atlantic (ERICA) field study: Objectives and plans. *Bull. Amer. Meteor. Soc.*, **69**, 1309–1320, https://doi.org/10.1175/1520-0477(1988)069<1309:TEORIC>2.0.CO;2.

Harrington, J. Y., K. Sulia, and H. Morrison, 2013a: A method for adaptive habit prediction in bulk microphysical models. Part I: Theoretical development. *J. Atmos. Sci.*, **70**, 349–364, https://doi.org/10.1175/JAS-D-12-040.1.

——, ——, and ——, 2013b: A method for adaptive habit prediction in bulk microphysical models. Part II: Parcel model corroboration. *J. Atmos. Sci.*, **70**, 365–376, https://doi.org/10.1175/JAS-D-12-0152.1.

Helms, C. N., M. L. Walker McLinden, G. M. Heymsfield, and S. R. Guimond, 2020: Reducing errors in velocity–azimuth display (VAD) wind and deformation retrievals from airborne Doppler radars in convective environments. *J. Atmos. Oceanic Technol.*, **37**, 2251–2266, https://doi.org/10.1175/JTECH-D-20-0034.1.

Herman, R. L., and Coauthors, 2020: Comparison of optimal estimation HDO/H_2O retrievals from AIRS with ORACLES measurements. *Atmos. Meas. Tech.*, **13**, 1825–1834, https://doi.org/10.5194/amt-13-1825-2020.

Heymsfield, A. J., S. Y. Matrosov, and N. B. Wood, 2016: Toward improving ice water content and snow-rate retrievals from radars. Part I: X and W bands, emphasizing *CloudSat*. *J. Appl. Meteor. Climatol*, **55**, 2063–2090, https://doi.org/10.1175/JAMC-D-15-0290.1.

——, A. Bansemer, A. Theis, and C. Schmitt, 2021: Survival of snow in the melting layer: Relative humidity influence. *J. Atmos. Sci.*, **78**, 1823–1845, https://doi.org/10.1175/JAS-D-20-0353.1.

Hines, P., J. Apt, and S. Talukdar, 2009: Large blackouts in North America: Historical trends and policy implications. *Energy Policy*, **37**, 5249–5259, https://doi.org/10.1016/j.enpol.2009.07.049.

Hock, T. F., and J. L. Franklin, 1999: The NCAR GPS dropwindsonde. *Bull. Amer. Meteor. Soc.*, **80**, 407–420, https://doi.org/10.1175/1520-0477(1999)080<0407:TNGD>2.0.CO;2.

Hou, A. Y., and Coauthors, 2014: The Global Precipitation Measurement mission. *Bull. Amer. Meteor. Soc.*, **95**, 701–722, https://doi.org/10.1175/BAMS-D-13-00164.1.

Houze, R. A., Jr., P. V. Hobbs, K. R. Biswas, and W. M. Davis, 1976: Mesoscale rainbands in extratropical cyclones. *Mon. Wea. Rev.*, **104**, 868–878, https://doi.org/10.1175/1520-0493(1976)104<0868:MRIEC>2.0.CO;2.

IHS Global Insight, 2014: The economic costs of disruption from a snowstorm. American Highway Users Alliance Rep., 9 pp., www.highways.org/2014/02/economic-impact-of-snowstorms/.

Jensen, A. A., J. Y. Harrington, H. Morrison, and J. A. Milbrandt, 2017: Predicting ice shape evolution in a bulk microphysics model. *J. Atmos. Sci.*, **74**, 2081–2104, https://doi.org/10.1175/JAS-D-16-0350.1.

Jurewicz, M. L., Sr., and M. S. Evans, 2004: A comparison of two banded, heavy snowstorms with very different synoptic settings. *Wea. Forecasting*, **19**, 1011–1028, https://doi.org/10.1175/WAF-823.1.

Keeler, J. M., B. F. Jewett, R. M. Rauber, G. M. McFarquhar, R. M. Rasmussen, L. Xue, C. Liu, and G. Thompson, 2016a: Dynamics of cloud-top generating cells in winter cyclones. Part I: Idealized simulations in the context of field observations. *J. Atmos. Sci.*, **73**, 1507–1527, https://doi.org/10.1175/JAS-D-15-0126.1.

——, ——, ——, ——, ——, ——, ——, and ——, 2016b: Dynamics of cloud-top generating cells in winter cyclones. Part II: Radiative and instability forcing. *J. Atmos. Sci.*, **73**, 1529–1553, https://doi.org/10.1175/JAS-D-15-0127.1.

——, ——, ——, ——, ——, ——, ——, and ——, 2017: Dynamics of cloud-top generating cells in winter cyclones. Part III: Shear and convective organization. *J. Atmos. Sci.*, **74**, 2879–2897, https://doi.org/10.1175/JAS-D-16-0314.1.

King, W. D., D. A. Parkin, and R. J. Handsworth, 1978: A hot-wired liquid water device having fully calculable response characteristics. *J. Appl. Meteor.*, **17**, 1809–1813, https://doi.org/10.1175/1520-0450(1978)017<1809:AHWLWD>2.0.CO;2.

Kocin, P. J., and L. W. Uccellini, 2004: *Snowstorms Along the Northeastern Coast of the United States: 1955–1985. Meteor. Monogr.*, No. 44, Amer. Meteor. Soc., 280 pp.

Kollias, P., E. Luke, M. Oue, and K. Lamer, 2020: Agile adaptive radar sampling of fast-evolving atmospheric phenomena guided by satellite imagery and surface cameras. *Geophys. Res. Lett.*, **45**, e2020GL088440, https://doi.org/10.1029/2020GL088440.

Korolev, A. V., J. W. Strapp, G. A. Isaac, and A. N. Nevzorov, 1998: The Nevzorov airborne hot-wire LWC–TWC probe: Principle of operation and performance characteristics. *J. Atmos. Oceanic Technol.*, **15**, 1495–1510, https://doi.org/10.1175/1520-0426(1998)015<1495:TNAHWL>2.0.CO;2.

Kroodsma, R. A., M. A. Fritts, J. F. Lucey, M. R. Schwaller, T. J. Ames, C. M. Cooke, and L. M. Hilliard, 2019: CoSMIR performance during the GPM OLYMPEX campaign. *IEEE Trans. Geosci. Remote Sensing*, **57**, 6397–6407, https://doi.org/10.1109/TGRS.2019.2906039.

Kumar, B., P. Götzfried, N. Suresh, J. Schumacher, and R. A. Shaw, 2018: Scale dependence of cloud microphysical response to turbulent entrainment and mixing. *J. Adv. Model. Earth Syst.*, **10**, 2777–2785, https://doi.org/10.1029/2018MS001487.

Kumjian, M. R., and K. A. Lombardo, 2017: Insights into the evolving microphysical and kinematic structure of northeastern U.S. winter storms from dual-polarization Doppler radar. *Mon. Wea. Rev.*, **145**, 1033–1061, https://doi.org/10.1175/MWR-D-15-0451.1.

——, S. A. Rutledge, R. M. Rasmussen, P. C. Kennedy, and M. Dixon, 2014: High-resolution polarimetric radar observations of snow-generating cells. *J. Appl. Meteor. Climatol.*, **53**, 1636–1658, https://doi.org/10.1175/JAMC-D-13-0312.1.

Lackmann, G. M., and G. Thompson, 2019: Hydrometeor lofting and mesoscale snowbands. *Mon. Wea. Rev.*, **147**, 3879–3899, https://doi.org/10.1175/MWR-D-19-0036.1.

Lamer, K., M. Oue, A. Battaglia, R. J. Roy, K. B. Cooper, R. Dhillon, and P. Kollias, 2021: Multifrequency radar observations of clouds and precipitation including the G-band. *Atmos. Meas. Tech.*, **14**, 3615–362, https://doi.org/10.5194/amt-14-3615-2021.

Lance, S., C. A. Brock, D. Rogers, and J. A. Gordon, 2010: Water droplet calibration of the cloud droplet probe (CDP) and in-flight performance in liquid, ice and mixed-phase clouds during ARCPAC. *Atmos. Meas. Tech.*, **3**, 1683–1706, https://doi.org/10.5194/amt-3-1683-2010.

Lawson, R. P., R. E. Stewart, and L. J. Angus, 1998: Observations and numerical simulations of the origin and development of very large snowflakes. *J. Atmos. Sci.*, **55**, 3209–3229, https://doi.org/10.1175/1520-0469(1998)055<3209:OANSOT>2.0.CO;2.

——, D. O'Connor, P. Zmarzly, K. Weaver, B. Baker, Q. Mo, and H. Jonsson, 2006: The 2D-S (Stereo) probe: Design and preliminary tests of a new airborne, high-speed, high-resolution particle imaging probe. *J. Atmos. Oceanic Technol.*, **23**, 1462–1477, https://doi.org/10.1175/JTECH1927.1.

Li, L., and Coauthors, 2015: The NASA High-Altitude Imaging Wind and Rain Airborne Profiler (HIWRAP). *IEEE Trans. Geosci. Remote Sensing*, **54**, 298–310, https://doi.org/10.1109/TGRS.2015.2456501.

Liao, L., R. Meneghini, A. Tokay, and L. F. Bliven, 2016: Retrieval of snow properties for Ku- and Ka-band dual-frequency radar. *J. Appl. Meteor. Climatol.*, **55**, 1845–1858, https://doi.org/10.1175/JAMC-D-15-0355.1.

Maahn, M., and P. Kollias, 2012: Improved Micro Rain Radar snow measurements using Doppler spectra post-processing. *Atmos. Meas. Tech.*, **5**, 2661–2673, https://doi.org/10.5194/amt-5-2661-2012.

Mace, G. G., and Q. Zhang, 2014: The CloudSat radar-lidar geometrical profile product (RL-GeoProf): Updates, improvements, and selected results. *J. Geophys. Res.*, **119**, 9441–9462, https://doi.org/10.1002/2013JD021374.

Mach, D. M., R. J. Blakeslee, M. G. Bateman, and J. C. Bailey, 2009: Electric fields, conductivity, and estimated currents from aircraft overflights of electrified clouds. *J. Geophys. Res.*, **114**, D10204, https://doi.org/10.1029/2008JD011495.

Mason, S. L., R. J. Hogan, C. D. Westbrook, S. Kneifel, D. Moisseev, and L. von Terzi, 2019: The importance of particle size distribution and internal structure for triple-frequency radar retrievals of the morphology of snow. *Atmos. Meas. Tech.*, **12**, 4993–5018, https://doi.org/10.5194/amt-12-4993-2019.

Matejka, T. J., R. A. Houze Jr., and P. V. Hobbs, 1980: Microphysics and dynamics of clouds associated with mesoscale rainbands in extratropical cyclones. *Quart. J. Roy. Meteor. Soc.*, **106**, 29–56, https://doi.org/10.1002/qj.49710644704.

Matrosov, S. Y., J. Heymsfield, and Z. Wang, 2005: Dual-frequency radar ratio of nonspherical atmospheric hydrometeors. *Geophys. Res. Lett.*, **32**, L13816, https://doi.org/10.1029/2005GL023210.

McFarquhar, G. M., G. Zhang, M. R. Poellot, G. L. Kok, R. McCoy, T. Tooman, A. Fridlind, and A. J. Heymsfield, 2007: Ice properties of single-layer stratocumulus during the Mixed-Phase Arctic Cloud Experiment: 1. Observations. *J. Geophys. Res.*, **112**, D24201, https://doi.org/10.1029/2007JD008633.

McGill, M. J., D. L. Hlavka, W. D. Hart, V. S. Scott, J. D. Spinhirne, and B. Schmid, 2002: The Cloud Physics Lidar: Instrument description and initial measurement results. *Appl. Opt.*, **41**, 3725–3734, https://doi.org/10.1364/AO.41.003725.

——, and Coauthors, 2004: Combined lidar-radar remote sensing: Initial results from CRYSTAL-FACE. *J. Geophys. Res.*, **109**, D07203, https://doi.org/10.1029/2003JD004030.

McMurdie, L. A., G. Heymsfield, J. E. Yorks, and S. A. Braun, 2019: Investigation of Microphysics and Precipitation for Atlantic Coast-Threatening Snowstorms (IMPACTS) collection. NASA EOSDIS Global Hydrology Resource

Center Distributed Active Archive Center, accessed 26 May 2021, https://doi.org/10.5067/IMPACTS/DATA101.

Midzak, N., J. E. Yorks, J. Zhang, B. van Diedenhoven, S. Woods, and M. McGill, 2020: A classification of ice crystal habits using combined lidar and scanning polarimeter observations during the SEAC4RS campaign. *J. Atmos. Oceanic Technol.*, **37**, 2185–2196, https://doi.org/10.1175/JTECH-D-20-0037.1.

Mitchell, D. L., 1988: Evolution of snow-size spectra in cyclonic storms. Part I: Snow growth by vapor deposition and aggregation. *J. Atmos. Sci.*, **45**, 3431–3451, https://doi.org/10.1175/1520-0469(1988)045<3431:EOSSSI>2.0.CO;2.

Mitrescu, C., J. M. Haynes, G. L. Stephens, S. D. Miller, G. M. Heymsfield, and M. J. McGill, 2005: Cirrus cloud optical, microphysical, and radiative properties observed during the CRYSTAL-FACE experiment: A lidar-radar retrieval system. *J. Geophys. Res.*, **110**, D09208, https://doi.org/10.1029/2004JD005605.

Morales, R. F., Jr., 2008: The historic Christmas 2004 south Texas snow event: Diagnosis of the heavy snow band. *Natl. Wea. Dig.*, **32** (2), 135–152, http://nwafiles.nwas.org/digest/papers/2008/Vol32No2/Pg135-Morales.pdf.

NASEM, 2018: *Thriving on Our Changing Planet: A Decadal Strategy for Earth Observation from Space.* National Academies Press, 716 pp., https://doi.org/10.17226/24938.

NCEI, 2020: State of the climate: National Climate Report 2020 winter highlights. Accessed 27 May 2021, www.ncdc.noaa.gov/sotc/national/202002#season-highlights.

Nicosia, D. J., and R. H. Grumm, 1999: Mesoscale band formation in three major northeastern United States snowstorms. *Wea. Forecasting*, **14**, 346–368, https://doi.org/10.1175/1520-0434(1999)014<0346:MBFITM>2.0.CO;2.

Novak, D. R., L. F. Bosart, D. Keyser, and J. S. Waldstreicher, 2004: An observational study of cold season–banded precipitation in northeast U.S. cyclones. *Wea. Forecasting*, **19**, 993–1010, https://doi.org/10.1175/815.1.

——, B. A. Colle, and S. E. Yuter, 2008: High-resolution observations and model simulations of the life cycle of an intense mesoscale snowband over the northeastern United States. *Mon. Wea. Rev.*, **136**, 1433–1456, https://doi.org/10.1175/2007MWR2233.1.

——, ——, and A. R. Aiyyer, 2010: Evolution of mesoscale precipitation band environments within the comma head of northeast U.S. cyclones. *Mon. Wea. Rev.*, **138**, 2354–2374, https://doi.org/10.1175/2010MWR3219.1.

Nystrom, R., S. J. Greybush, X. Chen, and F. Zhang, 2021: Potential for new constraints on tropical cyclone surface-exchange coefficients through simultaneous ensemble-based state and parameter estimation. *Mon. Wea. Rev.*, **149**, 2213–2230, https://doi.org/10.1175/MWR-D-20-0259.1.

Olson, W. S., and Coauthors, 2016: The microwave radiative properties of falling snow derived from nonspherical ice particle models. Part II: Initial testing using radar, radiometer and in situ observations. *J. Appl. Meteor. Climatol*, **55**, 709–722, https://doi.org/10.1175/JAMC-D-15-0131.1.

Oue, M., M. R. Kumjian, Y. Lu, J. Verlinde, K. Aydin, and E. E. Clothiaux, 2015: Linear depolarization ratios of columnar ice crystals in a deep precipitating system over the Arctic observed by zenith-pointing Ka-band Doppler radar. *J. Appl. Meteor. Climatol.*, **54**, 1060–1068, https://doi.org/10.1175/JAMC-D-15-0012.1.

——, P. Kollias, S. Y. Matrosov, A. Battaglia, and A. V. Ryzhkov, 2021: Analysis of the microphysical properties of snowfall using scanning polarimetric and vertically pointing multi-frequency Doppler radars. *Atmos. Meas. Tech.*, **14**, 4893–4913, https://doi.org/10.5194/amt-14-4893-2021.

Picca, J. C., D. M. Schultz, B. A. Colle, S. Ganetis, D. R. Novak, and M. J. Sienkiewicz, 2014: The value of dual-polarization radar in diagnosing the complex microphysical evolution of an intense snowband. *Bull. Amer. Meteor. Soc.*, **95**, 1825–1834, https://doi.org/10.1175/BAMS-D-13-00258.1.

Pisano, P. A., L. C. Goodwin, and M. A. Rossetti, 2008: U.S. highway crashes in adverse road weather conditions. *88th Annual American Meteorological Society Meeting*, New Orleans, LA, Amer. Meteor. Soc., 8.1, https://ams.confex.com/ams/88Annual/techprogram/paper_133554.htm.

Plummer, D. M., G. M. McFarquhar, R. M. Rauber, B. F. Jewett, and D. Leon, 2014: Structure and statistical analysis of the microphysical properties of generating cells in the comma-head region of continental winter cyclones. *J. Atmos. Sci.*, **71**, 4181–4203, https://doi.org/10.1175/JAS-D-14-0100.1.

——, ——, ——, ——, and ——, 2015: Microphysical properties of convectively generated fall streaks within the stratiform comma head region of continental winter cyclones. *J. Atmos. Sci.*, **72**, 2465–2483, https://doi.org/10.1175/JAS-D-14-0354.1.

Radford, J. T., G. M. Lackmann, and M. A. Baxter, 2019: An evaluation of snowband predictability in the High-Resolution Rapid Refresh. *Wea. Forecasting*, **34**, 1477–1494, https://doi.org/10.1175/WAF-D-19-0089.1.

Rauber, R. M., and Coauthors, 2014: Stability and charging characteristics of the comma-head region of continental winter cyclones. *J. Atmos. Sci.*, **71**, 1559–1582, https://doi.org/10.1175/JAS-D-13-0253.1.

——, S. M. Ellis, J. Vivekanandan, J. Stith, W.-C. Lee, G. M. McFarquhar, and B. F. Jewett, 2017: Finescale structure of a snowstorm over the northeastern United States: A first look at high resolution HIAPER Cloud Radar Observations. *Bull. Amer. Meteor. Soc.*, **98**, 253–269, https://doi.org/10.1175/BAMS-D-15-00180.1.

Rogers, R. R., and M. K. Yau, 1989: *A Short Course in Cloud Physics.* Pergamon Press, 304 pp.

Rosenow, A. A., D. M. Plummer, R. M. Rauber, G. M. McFarquhar, B. F. Jewett, and D. Leon, 2014: Vertical velocity and physical structure of generating cells and convection in the comma head region of continental winter cyclones. *J. Atmos. Sci.*, **71**, 1538–1558, https://doi.org/10.1175/JAS-D-13-0249.1.

——, R. M. Rauber, G. M. McFarquhar, and J. M. Keeler, 2018: Elevated potential instability in the comma head: Distribution and development. *Mon. Wea. Rev.*, **146**, 1259–1278, https://doi.org/10.1175/MWR-D-17-0283.1.

Ryzhkov, A., P. Zhang, H. Reeves, M. Kumjian, T. Tschallener, S. Trömel, and C. Simmer, 2016: Quasi-vertical profiles—A new way to look at polarimetric radar data. *J. Atmos. Oceanic Technol.*, **33**, 551–562, https://doi.org/10.1175/JTECH-D-15-0020.1.

Sanders, F., and L. F. Bosart, 1985: Mesoscale structure in the megalopolitan snowstorm, 11–12 February 1983. Part II: Doppler radar study of the New England snowband. *J. Atmos. Sci.*, **42**, 1398–1407, https://doi.org/10.1175/1520-0469(1985)042<1398:MSITMS>2.0.CO;2.

Schultz, C. J., and Coauthors, 2021: Remote sensing of electric fields observed within winter precipitation during the 2020 Investigation of Microphysics and Precipitation for Atlantic Coast-Threatening Snowstorms (IMPACTS) field campaign. *J. Geophys. Res. Atmos.*, **126**, e2021JD034704, https://doi.org/10.1029/2021JD034704.

Schultz, D. M., and P. N. Schumacher, 1999: The use and misuse of conditional symmetric instability. *Mon. Wea. Rev.*, **127**, 2709–2732, https://doi.org/10.1175/1520-0493(1999)127<2709:TUAMOC>2.0.CO;2.

——, and J. A. Knox, 2007: Banded convection caused by frontogenesis in a conditionally, symmetrically, and inertially unstable environment. *Mon. Wea. Rev.*, **135**, 2095–2110, https://doi.org/10.1175/MWR3400.1.

Skofronick-Jackson, G., and Coauthors, 2017: The Global Precipitation Measurement (GPM) mission for science and society. *Bull. Amer. Meteor. Soc.*, **98**, 1679–1695, https://doi.org/10.1175/BAMS-D-15-00306.1.

Spencer, R. W., R. E. Hood, F. J. LaFontaine, E. A. Smith, R. Platt, J. Galliano, V. L. Griffin, and E. Lobl, 1994: High-resolution imaging of rain systems with the Advanced Microwave Precipitation Radiometer. *J. Atmos. Oceanic Technol.*, **11**, 849–857, https://doi.org/10.1175/1520-0426(1994)011<0849:HRIORS>2.0.CO;2.

Trapp, J. R., D. M. Schultz, A. V. Ryzhkov, and R. L. Holle, 2001: Multiscale structure and evolution of an Oklahoma winter precipitation event. *Mon. Wea. Rev.*, **129**, 486–501, https://doi.org/10.1175/1520-0493(2001)129<0486:MSAEOA>2.0.CO;2.

Waitz, F., M. Schnaiter, T. Leisner, and E. Jarvinen, 2020: PHIPS-HALO: The airborne Particle Habit Imaging and Polar Scattering Probe—Part 3: Single particle phase discrimination and particle size distribution based on angular scattering function. *Atmos. Meas. Tech.*, **14**, 3049–3070, https://doi.org/10.5194/amt-14-3049-2021.

Walker McLinden, M. L., L. Li, G. M. Heymsfield, M. Coon, and A. Emory, 2021: The NASA/GSFC 94 GHz airborne solid-state Cloud Radar System (CRS). *J. Atmos. Oceanic Technol.*, **38**, 1001–1017, https://doi.org/10.1175/JTECH-D-20-0127.1.

Weinman, J. A., and P. J. Guetter, 1977: Determination of rainfall distributions from microwave radiation measured by the *Nimbus 6* ESMR. *J. Appl. Meteor. Climatol.*, **16**, 437–442, https://doi.org/10.1175/1520-0450(1977)016<0437:DORDFM>2.0.CO;2.

Wolfsberg, D. G., K. A. Emanuel, and R. E. Passarelli, 1986: Band formation in a New England winter storm. *Mon. Wea. Rev.*, **114**, 1552–1569, https://doi.org/10.1175/1520-0493(1986)114<1552:BFIANE>2.0.CO;2.

Yorks, J. E., D. L. Hlavka, W. D. Hart, and M. J. McGill, 2011: Statistics of cloud optical properties from airborne lidar measurements. *J. Atmos. Oceanic Technol.*, **28**, 869–883, https://doi.org/10.1175/2011JTECHA1507.1.

Yuter, S. E., and R. A. Houze Jr., 1995: Three-dimensional kinematic and microphysical evolution of Florida cumulonimbus. Part II: Frequency distributions of vertical velocity, reflectivity, and differential reflectivity. *Mon. Wea. Rev.*, **123**, 1941–1963, https://doi.org/10.1175/1520-0493(1995)123<1941:TDKAME>2.0.CO;2.

Zhang, F., C. A. Davis, M. L. Kaplan, and S. E. Koch, 2001: Wavelet analysis and the governing dynamics of a large-amplitude mesoscale gravity-wave event along the east coast of the United States. *Quart. J. Roy. Meteor. Soc.*, **127**, 2209–2245, https://doi.org/10.1002/qj.49712757702.

——, C. Snyder, and R. Rotunno, 2002: Mesoscale predictability of the "surprise" snowstorm of 24–25 January 2000. *Mon. Wea. Rev.*, **130**, 1617–1632, https://doi.org/10.1175/1520-0493(2002)130<1617:MPOTSS>2.0.CO;2.

——, S. E. Koch, and M. L. Kalpan, 2003: Numerical simulations of a large-amplitude mesoscale gravity wave event. *Meteor. Atmos. Phys.*, **84**, 199–216, https://doi.org/10.1007/s00703-002-0594-2.

——, Y. Weng, J. A. Sippel, Z. Meng, and C. H. Bishop, 2009: Cloud-resolving hurricane initialization and prediction through assimilation of Doppler radar observations with an ensemble Kalman filter. *Mon. Wea. Rev.*, **137**, 2105–2125, https://doi.org/10.1175/2009MWR2645.1.

Zhang, Y., D. J. Stensrud, and F. Zhang, 2019: Simultaneous assimilation of radar and all-sky satellite infrared radiance observations for convection-allowing ensemble analysis and prediction of severe thunderstorms. *Mon. Wea. Rev.*, **147**, 4389–4409, https://doi.org/10.1175/MWR-D-19-0163.1.